Transport and electrode reactions in magnesium-based electrochemical cells

Master Thesis

Joy Anne Kassandra Kieser

Justus-Liebig-Universität Gießen

Physikalisch-chemisches Institut

First Examiner: Prof. Jürgen Janek

Second Examiner: Prof. Vito Di Noto

19.09.2022

Selbstständigkeitserklärung

Hiermit versichere ich, die vorgelegte Thesis selbstständig und ohne unerlaubte fremde Hilfe und nur mit den Hilfen angefertigt zu haben, die ich in der Thesis angegeben habe. Alle Textstellen, die wörtlich oder sinngemäß aus veröffentlichten Schriften entnommen sind, und alle Angaben die auf mündlichen Auskünften beruhen, sind als solche kenntlich gemacht. Bei den von mir durchgeführten und in der Thesis erwähnten Untersuchungen habe ich die Grundsätze guter wissenschaftlicher Praxis, wie sie in der ‚Satzung der Justus-Liebig-Universität zur Sicherung guter wissenschaftlicher Praxis' niedergelegt sind, eingehalten. Entsprechend § 22 Abs. 2 der Allgemeinen Bestimmungen für modularisierte Studiengänge dulde ich eine Überprüfung der Thesis mittels Anti-Plagiatssoftware.

Datum	Unterschrift

Content

Content ..... **III**

List of abbreviations ..... **V**

List of Figures ..... **VI**

List of Tables ..... **X**

1 Introduction **1**

2 Basics **4**

2.1 Liquid electrolytes for Mg 5

2.2 The all-solid-state battery 6

2.3 Ion transport 7

2.4 Solid Electrolytes for Magnesium 9

2.5 NASICON 11

2.6 Hybrid electrolytes 13

3 Experimental **15**

3.1 Materials 15

3.2 Synthesis of $Mg_{0.5}Sn_2(PO_4)_3$ (MSP) powder 15

3.3 Preparation of the quasi-solid electrolytes (QSE) 15

3.4 Preparation of the ionic liquid electrolyte with $Mg(TFSI)_2$ conducting salt 16

3.5 Preparation of the ionic liquid electrolyte $Pyr_{14}Cl/(AlCl_3)_{1.5}$ IL without and with $MgCl_2$ 16

3.6 Cell-type 17

3.7 Conductivity measurements 18

3.8 E_a measurements 18

3.9 Electronic conductivity measurement 18

3.10 Electrochemical Stability Window (ESW) 19

3.11 Symmetrical Cell 19

3.12 Asymmetrical Cell 19

3.13 Powder XRD 19

3.14 SEM and EDX 20

3.15 FTIR 20

4 Methods 21

4.1 Conductivity 21

4.2 Electronic conductivity 21

4.3 E_a 21

5 Results and Discussion 22

5.1 MSP characterization 22

5.2 Electrochemical characterizations of QSE 26

5.2.1 Ratio Optimization 26

5.2.2 Chloride QSE with optimized ratio 32

5.3 QSE of 8:2 ratio with TFSI anion 37

5.3.1 FTIR 37

5.3.2 XRD 39

5.3.3 SEM and EDX 40

5.3.4 Electronic conductivity - DC polarization experiment 41

5.3.5 Electrochemical stability 42

5.3.6 Symmetrical Cell- RT and 200 cycle 43

5.3.7 Mg Plating Experiments 46

6 Conclusion & Outlook 57

7 Appendix 59

7.1 $MgCl_2$ 59

7.2 Arrhenius plot for the repeated E_a measurements 60

Bibliographical index 61

List of abbreviations

MSP: $Mg_{0.5}Sn_2(PO_4)_3$

EMIM TFSI: 1-Ethyl-3-methylimidazolium-bis(trifluormethylsulfonyl)imid

PYR14 TFSI: 1-Butyl-1-methylpyrrolidinium-bis(trifluoromethane sulfonyl)imid

$Mg(TFSI)_2$: Magnesium-bis(trifluoromethane sulfonyl)imid

THF: tetrahydrofuran

DME: dimethoxyethane

PEIS: Potentiostatic electrochemical impedance spectroscopy

LIB: Lithium-Ion-Battery

SE: solid-electrolyte

QSE: quasi-solid-electrolyte

SEI: solid-electrolyte interface

OCV: open circuit voltage

k_B: Boltzmann's constant

T: Temperature

σ: conductivity

List of Figures

Figure 1: Periodic table with mobile ions in blue, ligands in red, and cations that have been used to build crystal structures to provide ionic conduction in green. Taken from reference [31]. 7

Figure 2: Crystal structure of spinel AB_2X_4. Green depicted atoms are Se, Mg tetrahedra are brown, and Sc octahedra are depicted in grey. On the right is a schematic showing the pathway of Mg ion inside the spinel structure taken from reference [56] 11

Figure 3: (a) Crystal structure of rhombohedral NASICON $Mg_{0.5}Ti_2(PO_4)_3$ (left), with MgO_6 (brown), TiO_6 (green), and PO_4 polyhedra (grey).[68] (c) Simulated ion migration pathway in rhombohedral NASICON (yellow), and (b) stable (yellow) and metastable site (blue) of Mg in the rhombohedral NASICON structure, graphic taken from reference [63] 12

Figure 4: (a) Crystal structure of monoclinic NASICON from $Ni_{0.5}Zr_2(PO_4)_3$, with ZrO_6 (green) and PO_4 polyhedra (grey).[72] (c) Simulated ion migration pathway in monoclinic NASICON (yellow), and (b) stable (yellow) and metastable site (blue) of Mg in the monoclinic NASICON structure, graphic taken from reference [62] 13

Figure 5: Chemical structure of PYR_{14}, EMIM cation, and TFSI anion. 16

Figure 6: Schematic drawing of the cell. The graphic was taken from the supporting information from reference [72]. Instead of the all-solid-state battery (ASSB) pellet, only a QSE pellet was used. 17

Figure 7: Rietveld refinement of $Mg_{0.5}Sn_2(PO_4)_3$ based on the XRD pattern. 22

Figure 8: Crystal structure of MSP obtained from the Rietveld refinement, with PO_4 (grey), SnO_6 (blue), and MgO_6 (brown) polyhedra. 23

Figure 9: FTIR spectrum of MSP. 24

Figure 10: SEM images of MSP powder. On the left side picture with low magnification. Right picture of one particle with higher magnification. 25

Figure 11: High magnification SEM image of MSP powder. 25

Figure 12: Nyquist plot of MSP at 25 °C in the frequency range from 3 MHz to 100 mHz together with the fit and the equivalent circuit used for fitting. 26

Figure 13: Arrhenius plots showing the temperature dependent conductivity of different QSEs. 28

Figure 14: Nyquist plots of different PYR14 TFSI and EMIM TFSI QSE (a). Enlarged representation of the impedance spectra of ratio 9:1 (b), 8:2 (c), and 7:3 (d) recorded at room temperature with stainless steel as blocking electrodes. 30

Figure 15: Potential profiles of the Mg deposition-stripping in Mg/QSE/Mgsymmetrical cells measured at 60 °C with a current density of 1.57 µA·cm $^{-1}$ for the PYR14 TFSI QSEs of the different weight ratios.....31

Figure 16: Potential profiles of the Mg deposition-stripping in Mg/QSE/Mgsymmetrical cells measured at 60 °C with a current density of 1.57 µA·cm $^{-1}$ for the EMIM TFSI QSEs of the different weight ratios.....32

Figure 17: Nyquist plots of the [$PYR_{14}Cl/(AlCl_3)_{1.5}$] QSE without $MgCl_2$ and with 0.5 M $MgCl_2$ recorded at room temperature with stainless steel as blocking electrodes. 33

Figure 18: Arrhenius plots of the temperature-dependent conductivity used for determining the E_a of the [$PYR_{14}Cl/(AlCl_3)_{1.5}$] QSE without $MgCl_2$ and with 0.5 M $MgCl_2$. For determinating the E_a of the QSE without $MgCl_2$, experimental values above 40 °C were ignored because of a strong deviation from linearization. 34

Figure 19: Potential profiles of the Mg deposition-stripping in Mg/QSE/Mgsymmetrical cells measured at 60 °C with a current density of 1.57 µA·cm^{-1} for [$PYR_{14}Cl/(AlCl_3)_{1.5}$] QSE without $MgCl_2$ and with 0.5 M $MgCl_2$.....35

Figure 20: SEM image showing the Mg foil surface from the symmetric cell experiment with [$PYR_{14}Cl/(AlCl_3)_{1.5}$] 0.5 M $MgCl_2$ QSE at 60 °C plating and stripping experiment and related images with elemental mapping for Mg, Cl, O, C, Al, and P. This SEM picture was taken using the inlens detector. All following SEM images were taken with a secondary electron detector placed at an angle of 45° to the electron beam to get a better perception of the topology. 36

Figure 21: Comparison of normalized IR spectra of pristine MSP, ionic liquid electrolyte PYR14 TFSI, and QSE PYR14 TFSI of weight ratio 8:2. 38

Figure 22: Comparison of normalized IR spectra of pristine MSP, ionic liquid electrolyte EMIM TFSI, and QSE EMIM TFSI of weight ratio 8:2.....39

Figure 23: Comparison of powder XRD pattern from the pristine MSP powder with the QSEs of PYR14 and EMIM TFSI of 8:2 ratio. 39

Figure 24: SEM images of the QSEs left EMIM TFSI 8:2 and right PYR14 TFSI 8:2. 40

Figure 25: Current profile from DC polarization experiment for EMIM TFSI 8:2 QSE for the determination of the electronic conductivity. 41

Figure 26: Current profile from DC polarization experiment for PYR14 TFSI 8:2 QSE for the determination of the electronic conductivity.....42

Figure 27: Potential vs. steady-state current plots used to determine the electronic conductivity at 25 °C for EMIM and PYR14 TFSI 8:2 QSE. 42

Figure 28: Profile from the linear voltammetric sweep experiment to determine the electrochemical stability limit for the EMIM and PYR14 TFSI 8:2 QSE. The linear potential sweep was performed with a scan rate of 0.1 mV s^{-1}. The arrows indicate the direction of the anodic and cathodic sweep, measured separately with different cells. 43

Figure 29: Potential profiles of the Mg deposition-stripping in Mg/QSE/Mgsymmetrical cells measured at room temperature with a current density of 1.57 µA·cm^{-1} for EMIM and PYR14 TFSI 8:2. 44

Figure 30: Potential profiles of the Mg deposition-stripping in Mg/QSE/Mgsymmetrical cells measured at room temperature with a current density of 7.86 µA·cm^{-1} for EMIM and PYR14 TFSI 8:2. 45

Figure 31: SEM pictures oft he Mg foil of the EMIM TFSI 8:2 symmetric cell. Left picture Mg surface covered with electrolyte. Right, Mg foil of bare Mg surface with spots of the possible remaining deposit. In the middle, pictures of the EMIM TFSI 8:2 QSE (pellet diameter 10 mm) and Mg foil (diameter 9 mm) showing the side with the remaining deposit, marked with a red circle. 46

Figure 32: Voltage profile from the Mg plating experiment at room temperature using Al foil and a constant current of 1 µA. 47

Figure 33: Comparison of XRD pattern from the Al foil and the used QSE pellet of the EMIM TFSI 8:2 cell from the Mg plating experiment at room temperature and pristine MSP powder. 47

Figure 34: Comparison of XRD pattern from the Al foil and the used QSE pellet of the PYR14 TFSI 8:2 cell from the Mg plating experiment at room temperature and pristine MSP powder. 48

Figure 35: SEM with EDX elemental mapping images from Al foil showing the carbon-rich decomposition product from the PYR14 TFSI 8:2 cell used for the Mg plating experiment at room temperature. 49

Figure 36: SEM with EDX elemental mapping images from Al foil showing the carbon-rich decomposition product from the EMIM TFSI 8:2 cell used for the Mg plating experiment at room temperature. 50

Figure 37: SEM image of the corrosion found on the Al foil of the cells using EMIM TFSI (left) and PYR14 TFSI (right) QSE. 51

Figure 38: Voltage profile from the Mg plating experiment at 60 °C using Cu foil as plating substrate and a constant current of 5 µA. 52

Figure 39: Comparison of XRD pattern from the Cu foil and the used QSE pellet of the EMIM TFSI 8:2 cell from the Mg plating experiment at 60 °C and pristine MSP powder. 52

Figure 40: Comparison of XRD pattern from the Cu foil and the used QSE pellet of the PYR14 TFSI 8:2 cell from the Mg plating experiment at 60 °C and pristine MSP powder. 53

Figure 41: SEM images of the Cu foil used for Mg plating, left deposition found covering large areas of the Cu foil in the case of EMIM TFSI 8:2 QSE, and right PYR TFSI 8:2 cell Cu foil covered with QSE. 54

Figure 42: SEM image of Mg deposited on Cu foil for EMIM TFSI 8:2 QSE together with images of the elemental mapping from EDX. 55

Figure 43: SEM image of Mg deposited on Cu foil for PYR14 TFSI 8:2 QSE and images of the elemental mapping from EDX. 56

Figure 44: Comparison of XRD pattern from pristine crystallin $MgCl_2$ used as starting material, XRD pattern after first and second ball-milling.....59

Figure 45: Arrhenius plots showing the temperature dependent conductivity of QSEs PYR14 and EMIM TFSI 8:2 for measurement with 1.5 h and 3 h equilibration time for each temperature.....60

List of Tables

Table 1: Summary of all prepared QSEs with their used abbreviation. 16

Table 2: Structure parameters of MSP obtained by Rietveld refinement. 23

Table 3: Atomic ratio of different elements obtained from EDX mapping of pristine MSP. 24

Table 4: Total resistance and conductivity of MSP at 25 °C determined over the fit of the impedance spectra. 26

Table 5: Summary list of prepared QSE with EMIM TFSI and PYR14 TFSI ionic liquid electrolytes. 27

Table 6: Room temperature conductivity (25 °C) and E_a of the different QSEs. 28

Table 7: Summary list of prepared QSEs with Pyrrolidinium chloroaluminate ionic liquid. 33

Table 8: Room temperature conductivity (25 °C) and E_a of the $[PYR_{14}Cl/(AlCl_3)_{1.5}]$ QSE without $MgCl_2$ and with 0.5 M $MgCl_2$. 34

Table 9: Summary of results from the EDX elemental mapping. Atomic percentages for the QSE surface for EMIM and PYR14 TFSI QSE of 8:2 ratio. 40

Table 10: Electronic resistivity and calculated electronic conductivity from the DC polarization measurement. 41

1 Introduction

The global concern towards climate change calls for increasing energy production from renewable energy sources such as solar or wind power. The intermittent of these renewables requires a large energy storage capacity to stabilize the power grid and store overproduced electricity for utilization when needed. In addition, greater electrification of mobility also depends on batteries with high energy density and high safety. To this end, the lithium-ion battery (LIB), one of the most powerful and efficient energy storage technologies, was intensively researched, resulting in a higher energy density and bringing it closer to the theoretical maximum values. However, state-of-the-art LIBs have two bottleneck elements: Lithium and Cobalt, which struggle with the high cost and high toxicity, respectively. Hence, there is a need to find alternatives without these critical resources to satisfy the ever-increasing demand for LIBs. Therefore, searching for possible future battery systems has begun in the post-lithium battery field. An alternative candidate for the alkali metal lithium is the alkaline earth magnesium. But what are the advantages of using magnesium instead of lithium?

First of all, lithium only has a limited natural occurrence worthy of industrial extraction. The extraction is complicated due to a strong distribution in the earth's crust, with higher concentration in only a few regions. Specifically, about 57% of lithium resources are located in three countries alone, namely the Salar de Akagama in Chile, the Salar de Uyuni in Bolivia, and the Kings Mountain belt in the USA.[1] Here comes into view the widespread deposition of magnesium-rich minerals[2], securing raw material availability and reducing material cost. Second, the solid lithium electrode undeniably is the pinnacle of battery research regarding theoretical energy density. No other active anode material can offer a higher specific capacity concerning its light mass. But magnesium metal has the advantage of having a higher volumetric capacity due to its divalency. The theoretical volumetric capacity is 3832 $mAh \cdot cm^{-3}$ for magnesium metal and only 2062 $mAh \cdot cm^{-3}$ for lithium.[3] A battery can become smaller or store more energy at a comparable volume with this higher volumetric capacity.

Other than the advanced LIB, the secondary magnesium battery is still in the research stage to find suitable materials for the active parts of the battery, like electrolytes and

cathode materials. This is especially true for functional electrolytes. Aside from developing new liquid electrolytes compatible with the Mg anode, efforts are also made to develop a pure solid-state battery by replacing the flammable organic liquid electrolyte of the battery with a solid one to increase the safety of the energy storage systems. However, due to the strong coulombic interactions between the divalent Mg^{2+} and the host structure, the solid-electrolytes for Mg^{2+} today have very low ion conduction at moderate temperatures compared with current lithium and sodium ion conductors due to the high charge density of divalent Mg^{2+} ions.

As one of the promising Mg-ion conducting structures, oxide-based solid-state electrolytes have excellent stability but achieve acceptable conductivity only at high temperatures (e.g., $6.1 \cdot 10^{-3}$ S·cm^{-1} at 800 °C, for $Mg_{0.5}Zr_2(PO_4)_3$). One of the reasons is the high grain boundary resistance in these polycrystalline materials.[4] In order to reduce the grain boundary resistance, a quasi-solid-electrolyte (QSE) combining an oxidic solid magnesium electrolyte with an ionic liquid electrolyte is being considered. The main component of QSE is the polycrystalline solid electrolyte acting as a skeleton. The ionic liquid electrolyte is intended to improve the contact between the particles, aiding in ion transport across the particle boundaries. This concept was successfully employed for lithium QSEs showing promising results with the advantage of increased conductivity due to lower contact resistance. These QSEs consisted of lithium zirconate garnet ($Li_7La_3Zr_2O_{12}$) or a Natrium Super Ionic Conductor (NASICON)-type ceramic ($Li_{1.5}Al_{0.5}Ge_{1.5}(PO_4)_3$) in combination with a pyrrolidinium-bis(trifluoromethane-sulfonyl)imid ionic liquid.[5][6]

Inspired by the success of Li-QSEs, a Mg-QSE was explored for the first time in this thesis. A new NASICON-type solid $Mg_{0.5}Sn_2(PO_4)_3$ (MSP) was successfully prepared, which was combined with different ionic liquids, including two based on the bis(trifluoromethane-sulfonyl)imide (TFSI) anion with $Mg(TFSI)_2$ as conducting salt in a concentration of 1 mol L^{-1} with the different cations 1-Ethyl-3-methylimidazolium (EMIM), and 1-Butyl-1-methylpyrrolidinium (PYR14). Moreover, an ionic liquid with chloride was also explored. The ionic liquid was based on 1-Butyl-1-methylpyrrolidinium-chloride and aluminum chloride ($[PYR_{14}Cl/(AlCl_3)_{1.5}]$).[7] It was used without and with 0.5 mol L^{-1} $MgCl_2$ as conduction salt.

Three different weight ratios for the QSE with TFSI (MSP:IL ratio; 9:1, 8:2; 7:3) were evaluated. The activation energy (E_a) and conductivity were measured to assess how the electrolyte properties change with respect to ratio and cation type variation. Further study was performed on the selected 8:2 ratio and extended for another ionic liquid type with [$PYR_{14}Cl/(AlCl_3)_{1.5}$]. Electrochemical experiments with symmetrical and asymmetrical cells were carried out to investigate the QSEs further regarding their suitability as electrolytes and their performance parameters, including symmetrical cell overpotential for deposition and stripping, electrochemical stability, and electronic conductivity. The physical properties of the QSE were studied by several combined techniques: X-ray diffractometry (XRD) was used to determine the crystal structure of MSP with Rietveld refinement and to probe the structural stability of MSP in the QSEs. Fourier-transform infrared spectroscopy (FTIR), electron microscopy (SEM), and energy-dispersive X-ray spectroscopy (EDX) were used to characterize the electrolytes further. Morphologies of pristine QSEs and electrode surfaces after electrochemical experiments were analyzed with SEM and chemically characterized using EDX to understand the transfer properties of the Mg. Finally, the Mg conductivity of the QSEs was proven by Mg deposition.

2 Basics

The lithium-ion battery (LIB) is the state-of-the-art technology for secondary batteries. With the tremendous effort of development, current LIBs using layered oxide cathodes and graphite anodes are approaching the theoretical limit in terms of energy densities. The next step to increasing energy density is replacing the intercalation-type graphite anode with a metal anode to break this limit. One of the most challenging problems of solid lithium metal anodes is the formation of dendrites. They form upon subsequent stripping and plating of the anode metal. In each replating step, the metal is not evenly plated over the electrode surface due to the unevenly distributed current and eventually forms tree-like structures. In the worst case, these dendrite structures can penetrate the separator between the anode and cathode and short-circuit the battery.[8][9] Compared to Li, Mg-dendrites have a very high Young's modulus, increasing the risk of separator or solid electrolyte penetration.[8] But, with the right choice of electrolyte and working conditions, Mg can be electrodeposited, forming a smooth surface without dendrites.[10][11]

The development of electrolytes for Mg battery chemistries has been full of challenges compared with monovalent-ion-based batteries due to the sluggish solid-state diffusivity of the divalent Mg^{2+}. In LIBs, a solid electrolyte interface (SEI) is formed on the anode by the decomposition products of the carbonate electrolyte, which can effectively suppress the electron transfer and ultimately keep the electrolyte from continuous decomposition. Nevertheless, the interfacial layer formed on the Mg anode is impenetrable to Mg^{2+}.[12] For this reason, simply transferring the use of carbonate electrolyte solvent to Mg is not possible. Other solvents compatible with the Mg redox chemistry need to be employed. For example, etheric solvents like tetrahydrofuran (THF) are reduction stable against Mg metal. But there can also be a reduction of the conducting salt leading to surface passivation film formation. Similar to the layer formed by carbonate solvent, these surface films lead to high resistance and inhibit Mg stripping-plating.[12] In many cases, no Mg deposition is observable if the electrolyte is not sufficiently stable.[13] Nonetheless, if an electrolyte is found which is stable enough, Mg deposition-dissolution reaction can proceed with a very high coulombic efficiency, up to 100%.[14][15][16]

2.1 Liquid electrolytes for Mg

As discussed above, the liquid Mg electrolytes typically use ether or polyethers as solvents.[17] They are the only common solvent usable with magnesium's nucleophilic nature. Additional to the solvent, many different conducting salt types have been investigated. The lithium-ion battery 'standard' salts analogs for Mg like $Mg(ClO_4)_2$, $Mg(PF_6)$, or $Mg(CF_3SO_3)_2$ tend to passivate the Mg surface,[13][18][19] while electrodeposition of Mg from solutions of Grignard reagents (RMgX, R = alkyl or aryl group, X = halogen, Cl or Br) in ether is possible, known since 1927.[20] Mg can be reversibly stripped and plated from electrolytes comprising Grignard reagents dissolved in THF.[19][21][22] However, the etheric Gringard solutions are unstable against oxidation, and the anodic stability of 1-1.5 V vs. Mg/Mg^{2+} is too low for application in a battery. Additionally, they are not usable with intercalation cathodes. In the Grignard solutions, R_2Mg species form over the Schlenck equilibrium, which are reactive with the intercalation cathodes. Due to the depletion of the organomagnesium species, the Schlenk equilibrium is shifted, resulting in the precipitation of $MgCl_2$, which is electrochemically inactive.[23]

In 1990, Gregory et al. investigated different cathode materials for Mg intercalation and conduction salt/solvent combinations. Mg can either be reversibly electrodeposited or incorporated into an intercalation host, depending on whether the Mg salt in the electrolyte has a more covalent or ionic character. Large bulky anions can increase the readiness for ionic dissociation of the Mg salt and provide an opportunity to bring an electrolyte with a relatively high covalent character in an ionic form, necessary for intercalation. Gregory et al. concluded that a secondary Mg battery is technically realizable but requires further material engineering for electrolytes and higher voltage intercalation cathodes.[23] In 2000, Aurbach et al. reported an electrolyte of a 0.25 M solution of $Mg(AlCl_2BuEt)_2$ in THF, showing oxidational stability up to 2,5 V vs. Mg/Mg^{2+}.[17] Moreover, a prototype for a Mg-metal battery was reported comprising this electrolyte and the Chevrel-Phase $Mg_xMo_3S_4$ as an intercalation cathode in a coin cell setup.

The electrodeposition of Mg from electrolytes using magnesium halogenides is only possible by adding a lewis acid in molar ratio.[24] Lewis-acid-base pairs as electrolyte salts of the type R_xMgCl_{2-x} and R'_yAlCl_{3-y} with x = 0-2, y = 0-3 in THF were intensely studied by Auerbach et al.. [17][18][25] In these systems Mg deposition and dissolution is proceeding over a complex two-step mechanism. Involving the adsorption phenomena of Mg-species on the Mg surface, only a labile surface film is formed, which is not passivating the Mg surface.[21][26] Electrodeposition and dissolutions are reported to be able to proceed with high reversibility and efficiency.[14] But it is also possible for electrolytes containing chloride to passivate the Mg surface.[13] The drawback of Cl^- is nonetheless the corrosive nature towards non-noble metals so that there is corrosion of cell parts like stainless steel or aluminum current collectors at potentials over 2.5 V.[27] For this reason, work has also focused on chloride-free electrolytes for Mg. A prominent class of chloride-free electrolytes contains boron, introduced in 1990 by Gregory et al.[23] with $Mg(B(C_4H_9)_4)_2$ dissolved in THF and dimethoxyethane (DME). In another work, $Mg(BH_4)_2$ in DME was used by Mothadi et al. to utilize the strongly reducing property of borohydride to increase the stability with the strongly reducing Mg metal. The current density and coulombic efficiency (up to 94%) of the electrolyte could be improved with the addition of $LiBH_4$ (3.3:1 molar ratio $LiBH_4$:$Mg(BH_4)_2$). $LiBH_4$ weakens the interactions between BH_4^- and Mg^{2+} and improves the dissociation. The resulting electrolyte had anodic stability of 1.7-2.3 V vs. Mg/Mg^{2+}.[28]

2.2 The all-solid-state battery

The standard liquid electrolytes are volatile and flammable. These properties limit the temperature range where the batteries can operate safely. Despite the easier feasibility of liquid electrolytes, there is continued interest in developing solid-state batteries due to the prospect of increased safety. A ceramic solid electrolyte (SE) would further offer high thermal stability enabling battery use at elevated temperatures.[29][30]

As the most important part of the solid-state battery, the development of SE has received tremendous effort. Inorganic SEs usually consist of a rigid crystal skeleton formed by polyhedra built from metal or nonmetal elements (cation) in combination with a 'Ligand' (anion). The SEs contain one ionic species that can diffuse through the

skeleton structure. Figure 1 shows a periodic table with highlighted elements already used in SEs.[31] For solid-state Li batteries, there have already been reports of SEs which reach ion conductivities in the order of 10^{-2} S·cm^{-1} at room temperature. These are equal to the ionic conductivities of the currently used liquid electrolytes.[32] For example, $Li_{10}GeP_2S_{12}$, a SE for Li, shows ion conduction of 12 mS·cm^{-1} at 27 °C [33]; Li_2S-P_2S_5 glass ceramics, after densification with heat treatment to reduce grain resistance, reach a conductivity of 17 mS·cm^{-1}.[34]

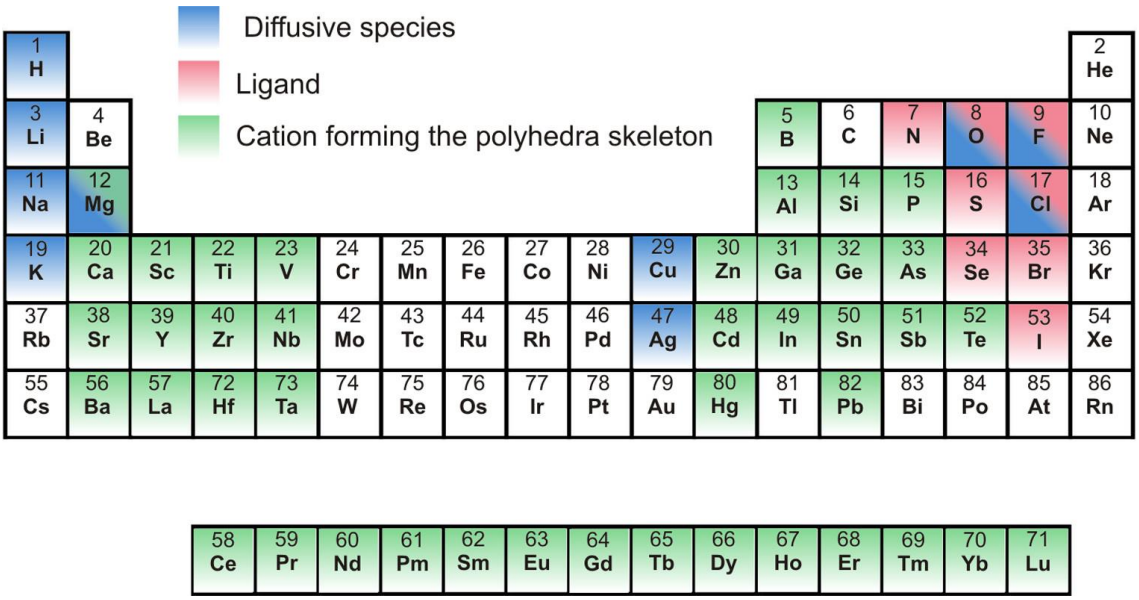

Figure 1 Periodic table with mobile ions in blue, ligands in red, and cations that have been used to build crystal structures to provide ionic conduction in green. Taken from reference [31].

2.3 Ion transport

In a liquid electrolyte, the transport number for the cation (e.g., Li^+, Na^+, Mg^{2+}) is below 0.5 due to the movable counter ions of the conducting salt. The smaller cations form a bigger solvation shell than the anions, which slows down their movement and leads to a larger fraction of the conductivity originating from the anions.[35] Besides the low transport number, a concentration gradient forms as the anions migrate perpendicularly to the cations. Therefore, liquid electrolyte cells face the problem of polarization limiting charging and discharging rates and concentration overpotentials.[36] In contrast, SE does not suffer from polarization, as the charges are better balanced, and no pronounced concentration gradient can occur. The counter ions are retained in the crystal lattice of

ceramic SE, giving transport numbers of unity.[37][38] For the SE, a smaller overall conductivity is sufficient with the higher transport number of the ions. For evaluating the feasibility of an SE, ionic conductivity and activation energies are two of the most important parameters, explained in the following.

The transport of the ions through a ceramic SE occurs over the hoping mechanism requiring defects (vacancies) or free interstitial positions.[39] The ions hop from their position in the lattice to the next accessible location. For this, a vacancy or free interstitial must be adjacent to the moving ion. The ions take the pathway of the lowest energy in the energetic landscape of the crystal lattice. The regular sites are local energetic minima separated by potential barriers (bottlenecks), as the energetic state of the moving ion depends on its coordinative environment. The energy needed to jump from one position to the next is the migration energy E_m. A low E_m indicates a good solid ion conductor and depends on the crystal structure. The activation energy for the ionic conduction E_a contains a contribution from E_m and an energy contribution for forming vacancies and interstitials. A good solid ion conductor should have a low E_a.

A variable factor affecting ionic conductivity is the number of defects in the lattice, which can be extrinsically increased by aliovalent doping.[40] The ionic conductivity is further related to the concentration of the migratory species. Usually, a parabolic behavior for ionic conductivity in relation to the concentration of migratory species is observed. Ionic conductivity increases until the optimal concentration is reached. The further increase in concentration will decrease conductivity due to increased interactions and lattice distortion.[41][42]

The ionic conduction in solids requires the expenditure of activation energy. With this, ionic conduction is temperature dependent like all activated processes. At higher temperatures, the SEs generally have higher ionic mobility and higher ionic conductivity. The temperature dependence of the ionic conduction ($\sigma(T)$) in the solid state can be described with equation (1), with B being a prefactor containing multiple terms, T being the absolute temperature in degree kelvin, and k_B the Boltzmann constant. The equation is derived from the random walk theory via the Nernst-Einstein relationship. In the random walk theory, ion conduction proceeds over occasional and randomly occurring

ion jumps between adjacent sites. The ions are considered to move independently of one another, and long-range electrostatic interactions are not considered.[39]

$$\sigma(T) = \frac{B}{T} \cdot exp\left(-\frac{E_a}{k_B T}\right) \quad (1)$$

2.4 Solid Electrolytes for Magnesium

Owing to the good safety of SEs, solid-state Mg-ion conductors have also been explored as an alternative option to liquid Mg electrolytes. However, grand challenges exist due to low Mg mobility at moderate temperatures.[43][44] The reason is that, although small ions are easier to move in solids, high-charged ions experience stronger polarization in the interaction of ion and counterion. Specifically, the Mg^{2+}-ion has an ionic radius of 0.86 Å[3]. It is small but has a very high charge density. For comparison, Li^+ has an ionic radius of 0.9 Å[3] and is only a monovalent ion. The hard Mg^{2+} ions strongly interact with the surrounding crystal lattice causing a slow diffusion in the solid state.

The aspiration for Mg-battery research is still to find a SE with sufficiently high ionic conductivity to be employed even at room temperature. The possibility of a Mg-SE started with Ikeda et al.'s first report of a Mg ion conducting solid in 1986. Magnesium zirconia phosphate $MgZr_4(PO_4)_6$ (MZP) has a reported ionic conductivity of $2.9 \cdot 10^{-5}$ S·cm^{-1} at 400 °C and $6.1 \cdot 10^{-3}$ S·cm^{-1} at 800 °C, respectively.[45] Improvements in ionic conduction in this system were achieved by Imanaka et al. by reducing grain boundary resistance by forming a composite with $Zr_2O(PO_4)_2$ as a microscopic dispersed second phase[46] and reducing bulk resistance by creating Mg^{2+} vacancies over substituting Zr^{4+} cation sites with higher valent Nb^{5+} cations.[47] Reaching conductivities of up to 10^{-2} S·cm^{-1} at 800 °C and 10^{-4} S·cm^{-1} at 500 °C.[47][48][28]

In 2013, Higashi et al. demonstrated that $Mg(BH_4)_2$ also has the capability to conduct Mg^{2+} ions. The ionic conductivity at 150 °C is 10^{-9} S·cm^{-1}, comparable to MZP. Moreover, an ionic conductivity higher by three magnitudes is obtained by substituting half of the borohydride with azanide resulting in a SE of the composition of $Mg(BH_4)(NH_2)$.[49] The partial substitution of BH_4^- with larger anions or neutral molecules reduces the binding

strength for Mg^{2+} to the anions, increasing the mobility. Kisu and Orimo et al. followed this strategy. They reported a magnesium borohydride ammonia borane SE ($Mg(BH_4)_2(NH_3BH_3)_2$) with a pure ionic conductivity of $1.3 \cdot 10^{-5}$ S·cm^{-1} at 30 °C, which is one of the highest for Mg-SE so far. Besides, reversible Mg plating on a Mo electrode is realized.[50] Unfortunately, the inherent disadvantage of this electrolyte is its low melting point. The electrolyte can only be used up to a maximum temperature of 45 °C. The electrolyte melt shows a high resistivity and thus can not be used as a molten salt electrolyte.

Inspired by lithium and sodium sulfide glass ceramics[51][52][53][54], Mg sulfide was also explored as a possible Mg-ion conductor. Tatsumisago et al. reported glass-ceramics with compositions $(100\text{-}x)(0.6MgS \cdot 0.4P_2S_5) \cdot x\ MgI_2$ ($0 \leq x \leq 30$) containing a crystallized $Mg_2P_2S_6$ phase having a maximum ionic conductivity of $2.1 \cdot 10^{-7}$ S·cm^{-1} at 200 °C. The conductivity increases with MgI_2 concentration due to the expanded lattice.[55]

DFT calculations by Ceder et al. for the MgX_2Z_4 spinels (X = S, Se, and Te; Z = Sc, In, and Y) led to great expectations of them being good Mg ion conductors. The crystal structure and the proposed Mg ion migration pathway in the spinels are displayed in Figure 2. Mg prefers the octahedral position in oxides and sulfides. But in the spinels, it is located in the tetrahedra position. During migration, the Mg ion moves from the less favored stable position in the tetrahedra site to the favored metastable octahedra side. This given coordination leads to low activation barriers of ion movement.[56] The calculations predicted shallow Mg migration barriers of ~ 400 meV. Experimentally, they successfully synthesized the $MgSc_2Se_4$ spinel. A high room temperature ionic conductivity of ~ 0.1 mS·cm^{-1} could be achieved, which is still considered the best performance up-to-date. However, a relatively high electronic conductivity of ~0.04% of the ionic conductivity was also observed, which could be attributed to intrinsic defects or impurity phases.[56] The mixed conductivity behavior makes the spinel $MgSc_2Se_4$ unsuitable as a Mg electrolyte. To enable practical application, efforts are still being made to reduce electronic conductivity.[57]

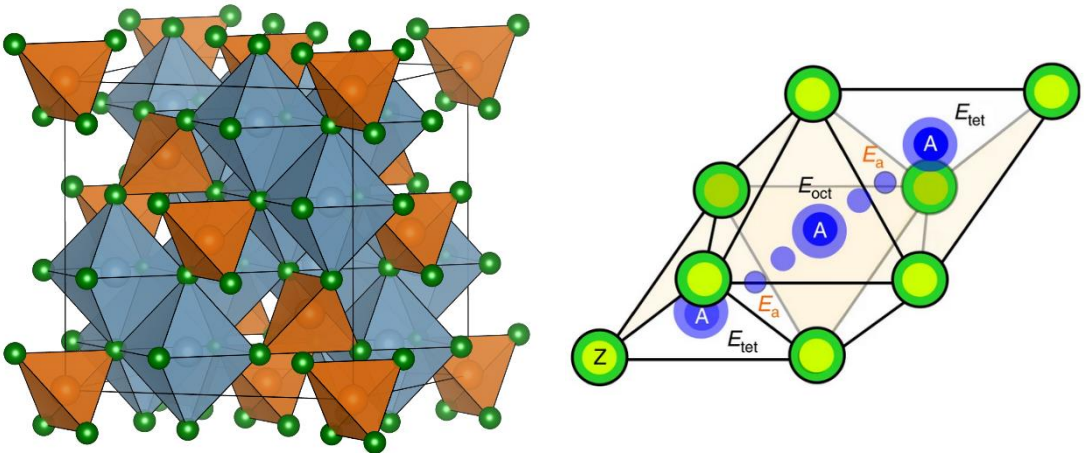

Figure 2 Crystal structure of spinel AB_2X_4. Green depicted atoms are Se, Mg tetrahedra are brown, and Sc octahedra are depicted in grey. On the right is a schematic showing the pathway of Mg ion inside the spinel structure taken from reference [56]

2.5 NASICON

The NAtrium Super Ionic CONductor (NASICON) structure was first reported by Goodenough et al. in 1976,[58] with the compounds of $Na_{1+x}Zr_2P_{3-x}Si_xO_{12}$ ($0 \leq x \leq 3$). The composition $Na_3Zr_2Si_2PO_{12}$ had the highest conductivity with ~ 10^{-4} S·cm^{-1} at room temperature and ~ 10^{-1} S·cm^{-1} at 300 °C.[58][59] The term NASICON originated from sodium conducting solids but is now used in a broader range to also describe derivates with other cations with the same or similar structure. NASICON is a polyanionic framework structure with the general formula $A_xM'(XO_4)_3$ (A = alkali, or earth alkali; M = transition metal). Examples of possible elements are A = Li, Na, K, Mg, Ca; M or M' = Fe, V, Ti, Zr, Sc, Mn, Nb, In, or Sn; X = S, P, Si, or As.[60] The structure comprises MO_6 ($M'O_6$) octahedra connected over shared corners to XO_4 tetrahedra. Two MO_6 ($M'O_6$) octahedra are linked over three XO_4 tetrahedra, forming a lantern unit $[(MO_6)_2(XO_4)_3]$. Depending on the arrangement of the lantern units, the NASICON structures can have two different crystal structures. One with monoclinic symmetry (space group $P2_1/n$), the second with a rhombohedral symmetry (space group $R\bar{3}c$), depicted in Figure 3 and Figure 4.[61] In the rhombohedral crystal, the structural lanterns are aligned along the c-axis of the hexagonal unit cell. Whereas in monoclinic symmetry, the lanterns are orientated in a zigzag form.[61] The NASICONS show morphotropism, as the structure can change with the composition.[61][58][62] Due to the greater structural symmetry, the

rhombohedral structure is expected to have a higher ionic conductivity than the monoclinic structure.[63] But the already studied Mg NASICONs have mostly monoclinic symmetry, including MZP.[64][65][66][67] The only known Mg type NASICON crystallizing in the rhombohedral space group $R\bar{3}c$ so far is $Mg_{0.5}Ti_2(PO_4)_3$.[68][69][70]

NASICON ceramics are rigid framework structures. The atoms that form the framework remain in their respective sites, while the mobile ions are located in extraframework positions (interstitials). The lantern units are three-dimensionally linked, forming the rigid crystal skeleton with large free interstitial spaces. The interstitials are connected by openings in the structure big enough to allow the passage of alkali- and earth-alkali-ions.[71] Simulated Mg migration pathways for rhombohedral and monoclinic NASICON structures are depicted in Figure 3 and Figure 4. The Mg ions can migrate in the NASICON structure via paths distributed three-dimensionally over the structure.

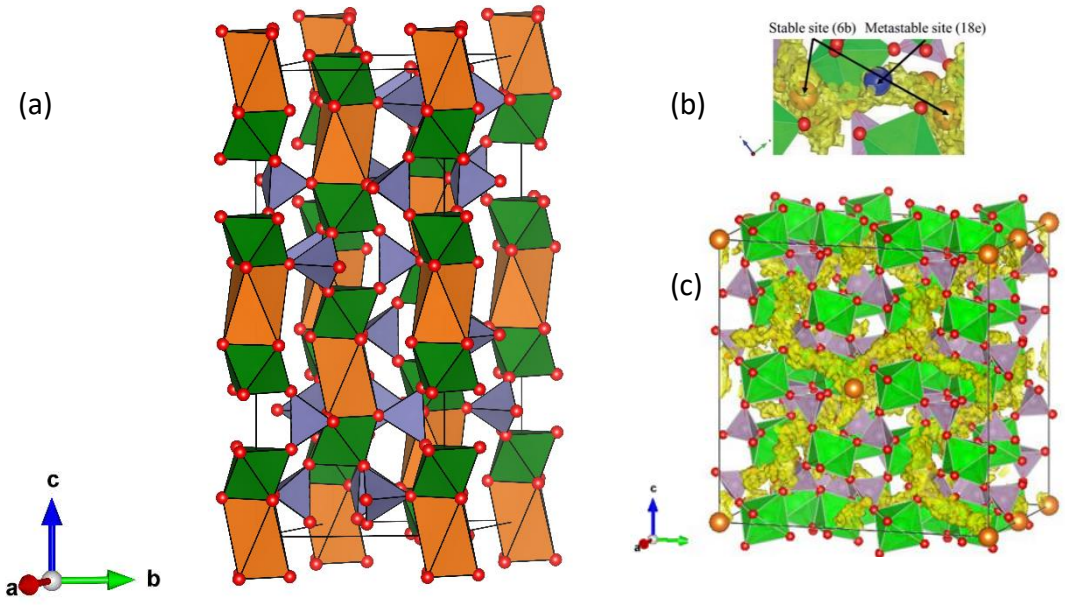

Figure 3 (a) Crystal structure of rhombohedral NASICON $Mg_{0.5}Ti_2(PO_4)_3$ (left), with MgO_6 (brown), TiO_6 (green), and PO_4 polyhedra (grey).[68] (c) Simulated ion migration pathway in rhombohedral NASICON (yellow), and (b) stable (yellow) and metastable site (blue) of Mg in the rhombohedral NASICON structure, graphic taken from reference [63]

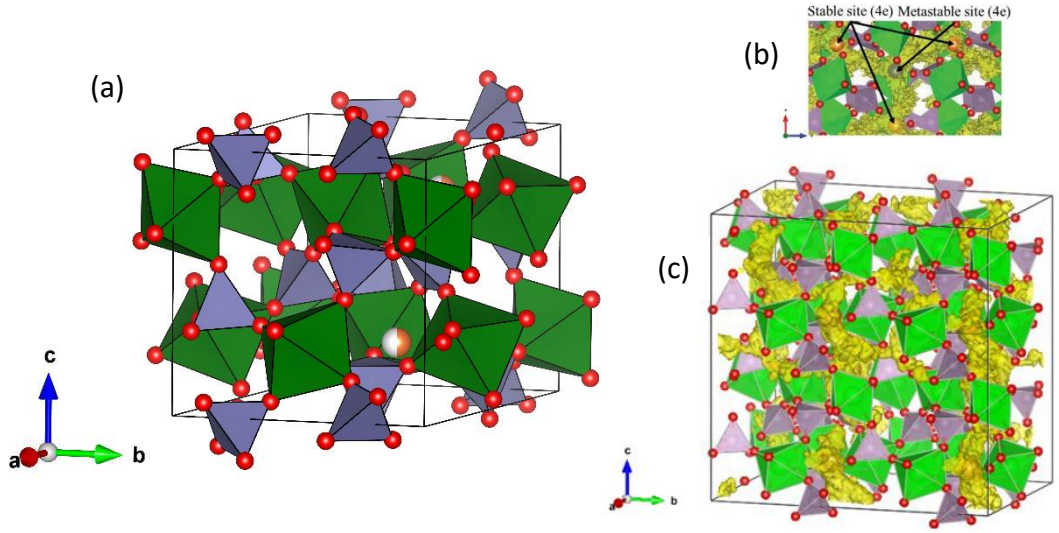

Figure 4 (a) Crystal structure of monoclinic NASICON from $Ni_{0.5}Zr_2(PO_4)_3$, with ZrO_6 (green) and PO_4 polyhedra (grey).[72] (c) Simulated ion migration pathway in monoclinic NASICON (yellow), and (b) stable (yellow) and metastable site (blue) of Mg in the monoclinic NASICON structure, graphic taken from reference [62]

2.6 Hybrid electrolytes

The Mg-NASICONs, like MZP, have only low conductivity. Their Li analogs also suffered from lower conductivities caused by insufficient conduction over grain/particle boundaries resulting in a high resistance for the SE. In the Li case, the problem could be mitigated by forming a hybrid electrolyte, a combination of two or more ion-conducting differentiable phases. In general, there are three electrolyte categories: liquid electrolytes, polymeric and inorganic solid electrolytes. Liquid electrolytes use a solvent, typically ethers, polyethers, or carbonates. More unusual are room temperature ionic liquids. A hybrid of an inorganic solid and an ionic liquid electrolyte in which the solid is the main component can be called a quasi-solid electrolyte (QSE). Successful attempts of the above quasi-solid electrolyte design can be found in garnet-type oxides, sulfides, and NASICON-type electrolytes. [72] In these hybrid electrolytes, the high grain boundary resistance of the pure SE was successfully mitigated.

As an example, Kim et al. reported QSEs using the ceramic $Li_7La_3Zr_2O_{12}$ (LLZO) in combination with 1-Butyl-1-methylpyrrolidinium-bis(trifluoromethane-sulfonyl)imid ($PYR_{14}TFSI$) and LiTFSI in an optimized weight ratio of 80:19:1. The QSE was prepared mechanically over mixing the components by gentle ball milling. The prepared QSE had excellent thermal stability of over 400 °C and electrochemical stability between 0.2 –

5.5 V vs. Li/Li^+, at a scan rate of 0.2 $mV \cdot s^{-1}$. The room temperature ionic conductivity of the QSE was $4 \cdot 10^{-4}$ $S \cdot cm^{-1}$, an improvement in conductivity of an order of two magnitudes compared to pure LLZO.[5]

The most recent work by Paolella and Krachkovskiy et al. used the NASICON-ceramic $Li_{1.5}Al_{0.5}Ge_{1.5}(PO_4)_3$ (LAGP), and 1-Propyl-1-methylpyrrolidinium-bis(trifluoromethane-sulfonyl)imid ($PYR_{13}TFSI$) in different weight ratios between 95:5 and 60:40 without Li salt. Paolella and Krachkovskiy et al. performed a more in-depth analysis of the reaction between the ceramic particles and the ionic liquid. A cation exchange reaction occurs between LAGP and $PYR_{13}TFSI$, forming LiTFSI salt. The formation of an ionic bridge between the particles takes place by adding 5-10% of the ionic liquid. The addition of extra LITFSI salt to the $PYR_{13}TFSI$ ionic liquid further increased the room temperature conductivity.[6]

3 Experimental

3.1 Materials

Following chemicals were used as purchased without further purification: Magnesium-Bis(trifluormethylsulfonyl)imid ($Mg(TFSI)_2$, TCI, >97%), 1-Ethyl-3-methylimidazolium-bis(trifluormethylsulfonyl)imid (EMIM TFSI, TCI, >98%), 1-Butyl-1-methylpyrrolidinium-bis(trifluoromethanesulfonyl)imid (PYR_{14} TFSI, TCI, >98%), $AlCl_3$ (anhydrous, ChemPur, >99.99%), 1-Butyl-1-methylpyrrolidinium-chloride (PYR14 Cl, TCI, >98%), $MgCl_2$ (Sigma-Aldrich, beads, 99.9%), Citric acid(anhydrous, Arcos organics, 99%), Magnesium acetate tetrahydrate (Alfa Aesar, 98%), Tin(II) chloride (Sigma-Aldrich, 98%), Ammonium dihydrogen phosphate (Alfa Aser, 98%), and Mg foil (Sigma-Aldrich 99.9%).

3.2 Synthesis of $Mg_{0.5}Sn_2(PO_4)_3$ (MSP) powder

The ceramic SE used was prepared with the sol-gel method. The chelating agent citric acid (1.9213 g, 10 mmol) was dissolved in 150 mL of demineralized water and mixed for 30 min. Then in this order, $Mg(Ac)_2{\cdot}4H_2O$ (0.4289 g, 2 mmol), $SnCl_2$ (1.51696 g, 8 mmol), and $NH_4H_2(PO_4)_3$ (1.38036 g, 12 mmol) were added with 30 min of mixing in between each. The solution was mixed for an additional 15 min. The beaker was covered with a paper tissue and heated in an oil bath at 90 °C to evaporate the water. The solid was pulverized with a mortar. The resulting powder was heated to 500 °C for 6 h (heating ramp 1 °C/min). After this, the heat was increased to 750 °C and held for an additional 6 h. After cooling, the resulting colorless powder was heated to 800 °C and sintered for 12 h.

3.3 Preparation of the quasi-solid electrolytes (QSE)

The ionic liquid and the hybrid electrolytes were handled and prepared under an inert argon atmosphere, with controlled water and oxygen contents below 5 ppm and 10 ppm. Solid electrolyte-ionic liquid electrolyte mixtures with weight ratios of 9:1, 8:2, and 7:3 were prepared by mixing MSP powder with the respective amount of ionic liquid electrolyte using a mortar (20 min). The following list summarizes the prepared QSE. Figure 5 shows the chemical structures of ions in the ionic liquid used in this work, followed by Table 1 summarizing the recipe for prepared QSEs.

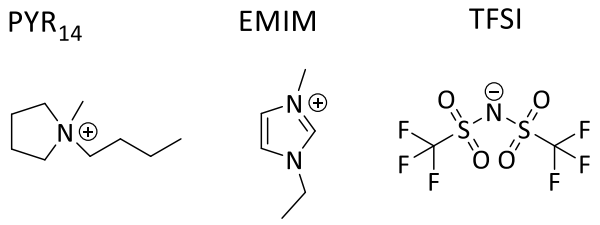

Figure 5 Chemical structure of PYR_{14}, EMIM cation, and TFSI anion.

Table 1 Summary of all prepared QSEs with their used abbreviation.

Sample abbreviation	Solid electrolyte	Mg-conducting salt	Ionic liquid cation	Ionic liquid anion	Weight ratio MSP:IL
EMIM TFSI 9:1	$Mg_{0.5}Sn_2(PO_4)_3$	1 M $Mg(TFSI)_2$	EMIM	TFSI	9:1
EMIM TFSI 8:2	$Mg_{0.5}Sn_2(PO_4)_3$	1 M $Mg(TFSI)_2$	EMIM	TFSI	8:2
EMIM TFSI 7:3	$Mg_{0.5}Sn_2(PO_4)_3$	1 M $Mg(TFSI)_2$	EMIM	TFSI	7:3
PYR14 TFSI 9:1	$Mg_{0.5}Sn_2(PO_4)_3$	1 M $Mg(TFSI)_2$	PYR_{14}	TFSI	9:1
PYR14 TFSI 8:2	$Mg_{0.5}Sn_2(PO_4)_3$	1 M $Mg(TFSI)_2$	PYR_{14}	TFSI	8:2
PYR14 TFSI 7:3	$Mg_{0.5}Sn_2(PO_4)_3$	1 M $Mg(TFSI)_2$	PYR_{14}	TFSI	7:3
PYR14 Cl	$Mg_{0.5}Sn_2(PO_4)_3$	––	$PYR_{14}Cl$	1.5 $AlCl_3$	8:2
PYR14 Cl MgCl2	$Mg_{0.5}Sn_2(PO_4)_3$	0.5 M $MgCl_2$	$PYR_{14}Cl$	1.5 $AlCl_3$	8:2

3.4 Preparation of the ionic liquid electrolyte with $Mg(TFSI)_2$ conducting salt

The EMIM TFSI and PYR14 TFSI ionic liquid electrolytes were prepared with $Mg(TFSI)_2$ at a concentration of 1 mol L^{-1}. To 0.585 g of $Mg(TFSI)_2$, 1 mL of the IL was added and left on a hot plate at 100 °C for homogenization for at least 2 h.

3.5 Preparation of the ionic liquid electrolyte $Pyr_{14}Cl/(AlCl_3)_{1.5}$ IL without and with $MgCl_2$

Pyrrilidinium haloaluminate ionic liquid was prepared by slowly adding $AlCl_3$ to $Pyr_{14}Cl$ with amounts adequate for a molar ratio of 1:1.5 of $Pyr_{14}Cl$ to $AlCl_3$. The resulting ionic liquid was mixed overnight.[7] An electrolyte with 0.5 mol L^{-1} concentration of $MgCl_2$ was

prepared by adding the required amount of ball-milled $MgCl_2$ to 1 mL of IL. The grinding conditions for $MgCl_2$ are described in more detail in the appendix. The mixture was left on a hot plate (100 °C) for 5 h until homogenization. After cooling to room temperature, the IL became a gel-like consistency. For making the QSE, the IL was heated on a hotplate (for 30 min) until it was liquid.

3.6 Cell-type

All electrochemical measurements were performed using a two-electrode cell. The built-up of the in-house made cell casing is already described in the literature[73] and depicted in Figure 6. The cell comprises a brass cell casing with an insulating polyetheretherketone (PEEK) housing inside the casing. About 80 mg of solid electrolyte powder was pressed into a pellet in the PEEK housing using uniaxial pressing, with a pressure of 3 metric tons for 3 min. The resulting electrolyte pellet has a diameter of 10 mm and a thickness between 0.3 to 0.55 mm. The stainless steel pistons were used as current collectors. In case, a metal foil was used as an electrode. The foil was placed between the QSE and the stainless steel piston after the QSE pellet was pressed. The completed cell was pressed again at 3 T for 1 min to ensure good contact. In the case of a Mg electrode (diameter 9 mm, thickness 0.1 mm), the magnesium oxide layer was manually removed by scratching with a scalpel before electrodes were punched out from the Mg metal sheet. During measurement, the cell was fixed in a metal frame with a screw tightened with a torque of 10 Nm.

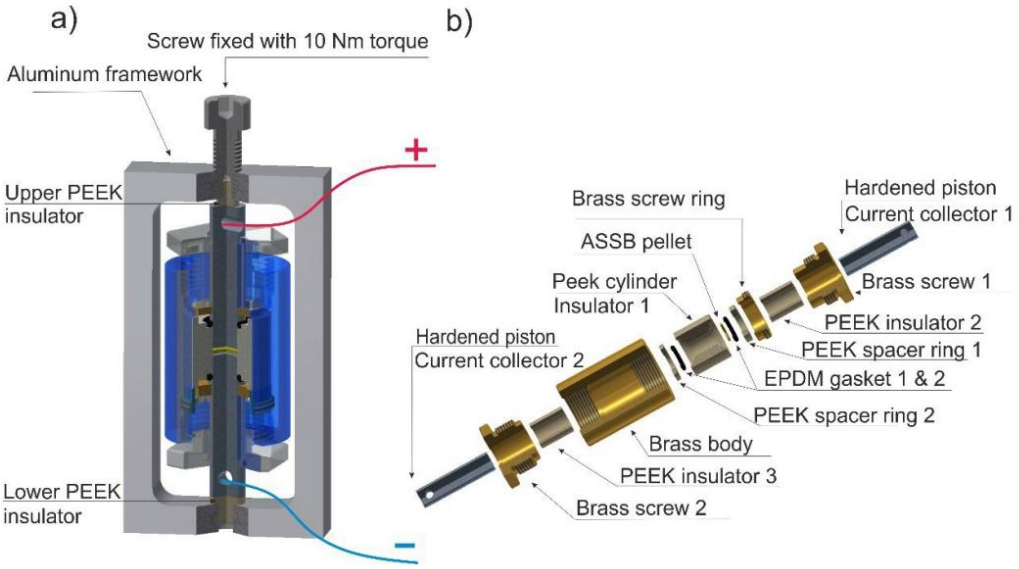

Figure 6 Schematic drawing of the cell. The graphic was taken from the supporting information from reference [72]. Instead of the all-solid-state battery (ASSB) pellet, only a QSE pellet was used.

3.7 Conductivity measurements

The conductivity was determined with electrochemical impedance spectroscopy measurements with a perturbation of the potential (PEIS) using a Biologic VMP300 or VMP3 potentiostat. The above-described cell setup was used with the stainless steel pistons as Mg ion blocking electrodes. Measurements were performed within the frequency range of 1 MHz to 100 mHz by applying a 100 mV amplitude voltage.

The electrolyte pellet thickness was measured after impedance measurement to calculate the conductivity. The bulk resistance could be directly obtained from the Nyquist plots of the impedance measurements, further described in the method section. For pristine MSP, the resistance was determined by fitting the impedance spectra with an equivalent circuit using the impedance analysis software RlaxIS3 from rhd instruments.

3.8 E_a measurements

The activation energy for conduction was determined with temperature-controlled impedance measurements at different temperatures between -40 to 60 °C/ 80 °C at intervals of 10 °C or 5 °C with the before mentioned cell setup inside a climate chamber. In the beginning, during, and at the end of the measurement, impedance spectra at 25 °C were recorded for comparison. Between measurement, the cell rested at an open circuit potential (OCV) for 1.5 h to equilibrate at the set temperature. The calculation of the E_a is further described in the following method section.

3.9 Electronic conductivity measurement

Chronoamperometry measurements were performed at 25 °C. A fixed potential was applied and held for 1 h while recording the resulting electrical current. This was repeated at different potentials between 0.1 V and 2 V. The steady-state current was used to obtain the electrical resistance of the QSE used for calculating the electrical conductivity. The calculation is further described in the method section. Used electrodes were the stainless steel pistons.

3.10 Electrochemical Stability Window (ESW)

The cell assembly for ESW measurement consisted of the QSE pellet with one Mg foil on one side and the bare stainless steel piston on the other. The Mg side worked simultaneously as a reference and counter electrode, while the stainless steel side functioned as the working electrode. A potential sweep in the anodic region was performed at a scan rate of 0.1 mV s^{-1} to 5 V vs. Mg/Mg^{2+} starting from OCV to test the oxidation stability of the QSE. With another cell, a potential sweep in the cathodic region was performed at the same scan rate from OCV to -5 V vs. Mg/Mg^{2+} to test the reduction stability of the QSE.

3.11 Symmetrical Cell

A piece of Mg metal foil was added on both sides of the cell-setup between the electrolyte and the stainless steel contact pistons for the symmetrical cell experiment. Plating and stripping Mg metal experiments were performed at a temperature of 60 °C or room temperature (RT). 50 or 200 cycles of chronopotentiometric deposition and stripping of Mg with a current of 1 µA or 5 µA (corresponding to a current density of 1.57 µA·cm^{-1} or 7.86 µA·cm^{-1}) were performed for 30 min in each direction.

3.12 Asymmetrical Cell

The experiment for plating of Mg metal was performed at RT or inside a climate chamber at 60 °C with the same cell setup as the symmetrical cell experiments, except that on one side, the Mg foil was substituted with an Al or Cu foil with a diameter of 10 mm. For plating of Mg, the cell was first cycled with a current of 1 µA for 30 min for 5 cycles before Mg was deposited on the Al or Cu foil with a constant current.

3.13 Powder XRD

X-ray diffraction measurements were performed on a PANalytical Empyrean Series 2 X-ray diffraction system with Bragg-Brentano geometry using Cu-Kα irradiation ($K\alpha_1$ wavelength 1.5405980 Å and $K\alpha_2$ wavelength 1.5444260 Å with a $K\alpha_2/K\alpha_1$ ratio of 0.500) with a source potential of 40 kV and current of 40 mA. Monocrystalline silicon sample holders were used, which were covered airtight with kapton-foil for air-sensitive samples.

Rietveld refinement of the MSP powder was carried out using the FullProf Suite (version January 2021) within a 2θ range from 10° to 70°. The peak profiles were described with the Thompson-Cox-Hastings pseudo-Voigt function[74] convoluted with a function for axial divergence asymmetry[75]. The background was linearly interpolated between manually set points.

3.14 SEM and EDX

The surfaces of the electrodes (Mg, Al, or Cu foil) and the electrolytes were studied with a Zeiss electron microscope (Merlin) and equipped with an EDX detector (X-Max 50 Silicon Drift Detector). The secondary electron detector of the SEM was used. Samples were fixated with Cu-tape on top of the sample holder. A small piece of the electrode was cut and used without further preparation for ex-situ measurements of cell electrodes. The samples were transferred from the glovebox to the SEM chamber via a Leica transfer module (EM VCT 500) to avoid air contamination.

EDX elemental mapping was performed with an electron beam acceleration voltage of 6 kV and a current of 2 nA. Atomic percentages are taken from three different spectra from different SE particles, and the average value was reported with standard deviation.

3.15 FTIR

Fourier-transform infrared spectra were recorded on an ATR Nicolet iS5 spectral photometer in the mid-infrared region from 4000 cm^{-1} to 550 cm^{-1}. For measurement, the QSE powder was pressed into a pellet with a hand pressing tool. The spectrometer is located in an argon-filled glovebox.

4 Methods

4.1 Conductivity

Using the following formula (2), the ionic conductivity σ is calculated from the resistance *R* obtained from the impedance measurement. *R* is directly taken from the Nyquist plot representation of the data as the real conductivity value at the point where the semicircle at high frequency enters into the line at the lower frequencies.[76] With *A* being the electrode area and *d* the pellet thickness.

$$\sigma = \frac{1}{R} \cdot \frac{d}{A} \tag{2}$$

4.2 Electronic conductivity

The electronic conductivity σ_{el} is calculated similarly to σ, namely with the electrical resistance R_{el} obtained from chronoamperometric measurement according to equation (3). With the geometrical parameters *A* the electrode area, and *d*, the pellet thickness.

$$\sigma_{el} = \frac{1}{R_{el}} \cdot \frac{d}{A} \tag{3}$$

By plotting the applied potential against the steady-state current values, the slope of the graph represents the resistance known over Ohm's law.

$$R_{el} = \frac{U}{I} \tag{4}$$

4.3 E_a

The activation energy was determined over impedance measurements at different temperatures. The conductivity at the different temperatures was determined as described above. The activation energies were determined by plotting ln(σT) against 1000/T using equation (5) derived from equation (1). E_a is obtained from the slope of the graph by linear fitting.

$$\ln(\sigma T) = \ln(B) - \frac{E_a}{k_B T} \tag{5}$$

5 Results and Discussion

5.1 MSP characterization

The used SE is a newly synthesized Mg NASICON and has not yet been described in the literature. This is the first characterization of this compound, so the structure is refined with the Rietveld refinement method using powder XRD data. It is further characterized by using FTIR, SEM, and EDX techniques.

For the refinement of MSP, rhombohedral symmetry is assumed. Initial atomic coordinates for the structure refinement were derived from $Mg_{0.5}Ti_2(PO_4)_3$[68] and $NaSn_2(PO_4)_3$[77]. The refined structure parameters are reported in Table 2. The refinement shows that the synthesized MSP is not phase pure and contains at least one impurity phase, likely SnP_2O_7. The precise determination and quantification of the impurity phase will need further investigation. Figure 7 shows the experimental XRD pattern together with the pattern calculated from the refinement.

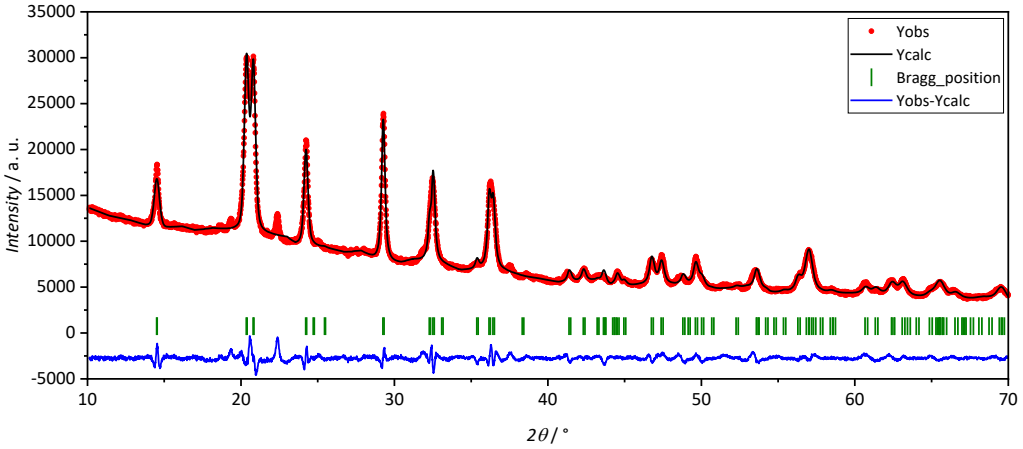

Figure 7 Rietveld refinement of $Mg_{0.5}Sn_2(PO_4)_3$ based on the XRD pattern.

The identified main phase of MSP has rhombohedral symmetry and the $R\bar{3}c$ space group. The framework structure is formed by PO_4-tetrahedra corner-linked with SnO_6-octahedra. Mg ions are coordinated within MgO_6 units in trigonal antiprismatic coordination. The MgO_6 units share faces with two SnO_6-octahedra and are oriented along the c-axis of the crystal unit cell. In MSP, the Mg sites are only partially occupied.

The Mg sites are occupied to 50% for the stoichiometry of $Mg_{0.5}Sn_2(PO_4)_3$. Figure 8 shows the unit cell of the crystal structure of MSP.

Table 2 Structure parameters of MSP obtained by Rietveld refinement.

	Unit cell parameters
	$Mg_{0.5}Sn_2(PO_4)_3$
Crystal structure	rhombohedral
space group	167
a / Å	8.53821
b / Å	8.53821
c / Å	21.59820
V / Å³	1363.5838
α / °	90.0°
β/ °	90.0°
γ / °	120.0°
Agreement factors	
Weight R-profile, R_{wp}	3.32
R-profile, R_p	2.42
χ^2	8.9935

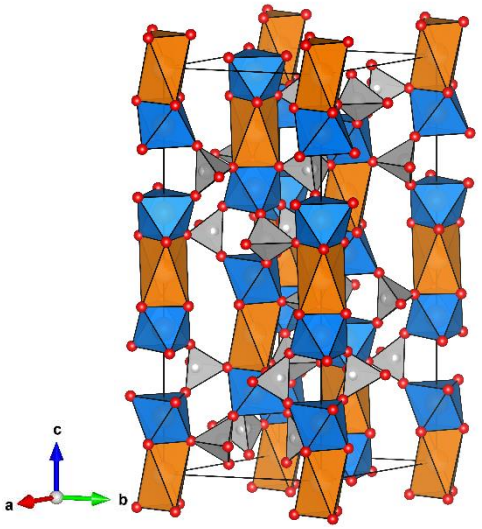

Figure 8 Crystal structure of MSP obtained from the Rietveld refinement, with PO_4 (grey), SnO_6 (blue), and MgO_6 (brown) polyhedra.

The vibrations of the phosphate group dominate the FTIR spectrum of MSP displayed in Figure 9. In the 1250-900 cm^{-1} region are symmetric and asymmetric stretching vibrations of the P–O bonds. Ranging from 670-550 cm^{-1} are the asymmetric bending modes of O-P-O from the PO_4^{3-} anions.[65][78][79][80] Within the FTIR spectra, vibrations of the possible impurity component SnP_2O_7 can not be distinguished from the phosphate group of MSP. The vibrations of the diphosphate group are in the same range covered by the broad peak attributed to the stretching vibrations of the PO_4^{3-} anion. The other absorption bands are discussed in more detail in the following section, together with the FTIR spectra of the QSEs.

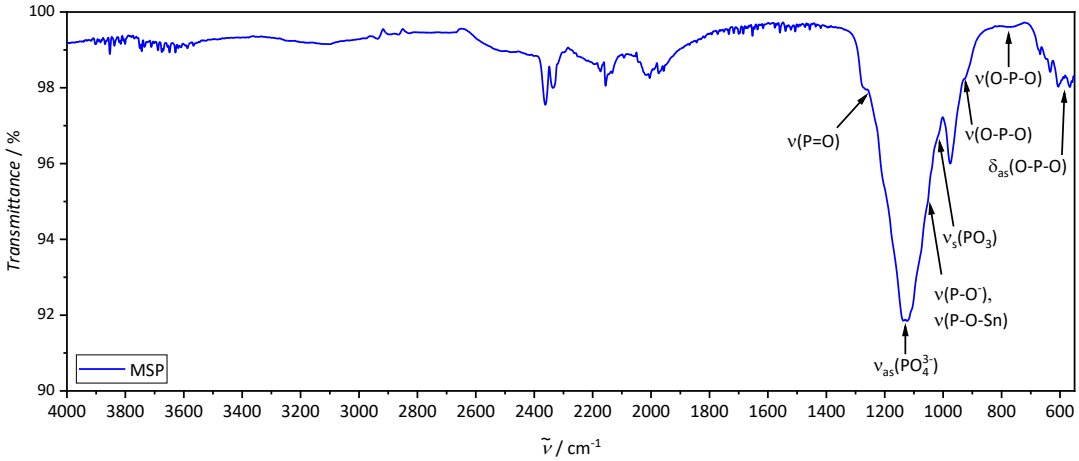

Figure 9 FTIR spectrum of MSP.

The morphology of the MSP powder is further studied with SEM. The prepared pristine MSP is very porous due to the applied chelating agent. This favors the penetration of ionic liquid for the preparation of QSEs. The morphology of MSP, as shown in Figure 10 and Figure 11, consists of small grains agglomerated to different-sized bigger particles that are randomly shaped with rounded edges. With EDX, elemental mapping is performed on the MSP particles. The determined atomic ratios, summarized in Table 3, agree with the stochiometry used in the synthesis, while the excess of Sn also suggests the existence of a secondary impurity phase. Small contamination with carbon is detected, which might originate from the glue on the Cu-tape used for sample preparation. Since the determination of atomic ratios with EDX is restricted to the surface region, the composition analysis with EDX is susceptible to surface contamination.

Table 3 Atomic ratio of different elements obtained from EDX mapping of pristine MSP.

$Mg_{0.5}Sn_2P_3O_{12}$	**O/Atom%**	**P/Atom%**	**Sn/Atom%**	**Mg/Atom%**	C/**Atom%**
Theoretical	68.6	17.1	11.4	2.9	0
Average	63.1	17.1	15.1	2.7	2.0
Standard deviation	3.9	1.2	1.5	0.2	1.8

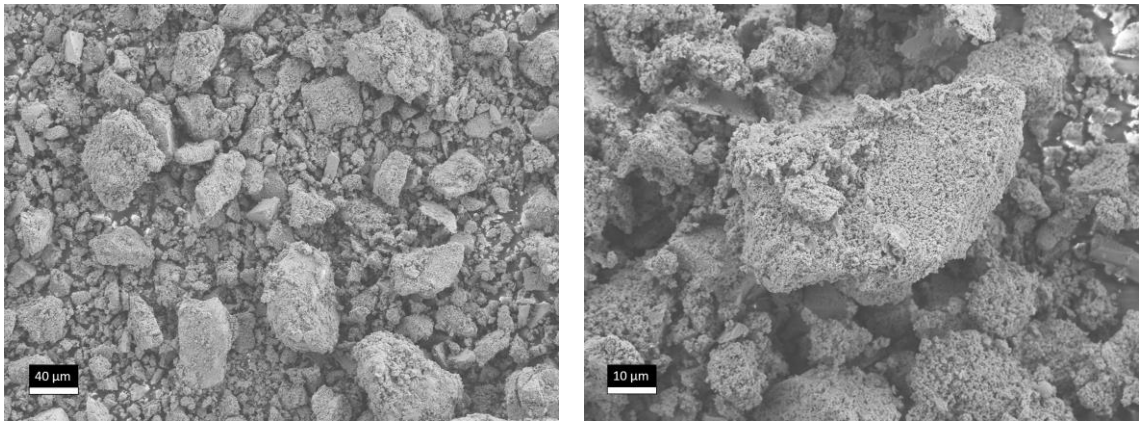

Figure 10 SEM images of MSP powder. On the left side picture with low magnification. Right picture of one particle with higher magnification.

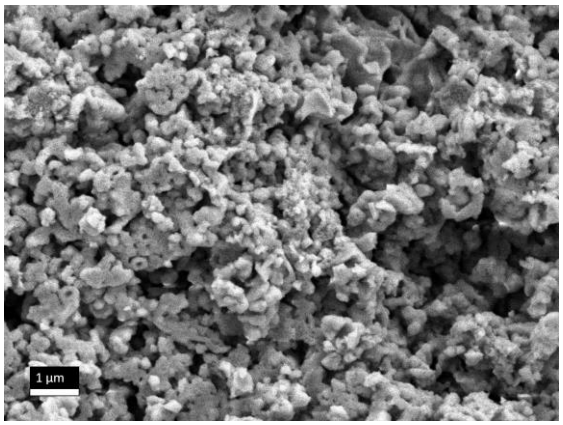

Figure 11 High magnification SEM image of MSP powder.

The Nyquist plot for the MSP impedance consists of a depressed semicircle, depicted in Figure 12. The impedance spectrum was fitted with a simple equivalent circuit based on a constant phase, a resistor, and a capacitor element in parallel.

Based on the fitted result, the synthesized MSP has a very high resistance at 25 °C with a conductivity of only $1.7 \cdot 10^{-11}$ S·cm$^{-1,}$ a typical property of oxide Mg-ion conductors at room temperature. Apart from the high Mg^{2+} transport barrier in the bulk material, a factor contributing to the high room temperature resistivity might be a contact problem between the MSP pellet and the stainless steel current collectors. Two cells were built for the measurement. Both cells needed to be pressed twice because the contact between the MSP pellet and the stainless steel current collector was broken. The disrupted contact in the cell was evident from a cell voltage of approximately 2 V, inexplicably high for a cell sandwiching a solid electrolyte pellet between two stainless

steel electrodes. The results show the already known problems of oxide Mg ion conductors of having vanishing ion conduction at ambient temperature and showing contact problems between the electrode and solid electrolyte, which are related to the high grain boundary resistance of the oxides.[4]

Table 4 Total resistance and conductivity of MSP at 25 °C determined over the fit of the impedance spectra.

	R / Ω	σ (25 °C) / S·cm^{-1}
$Mg_{0.5}Sn_2(PO_4)_3$	$4.13 \cdot 10^9 \pm 6 \cdot 10^8$	$1.70 \cdot 10^{-11} \pm 2 \cdot 10^{-12}$

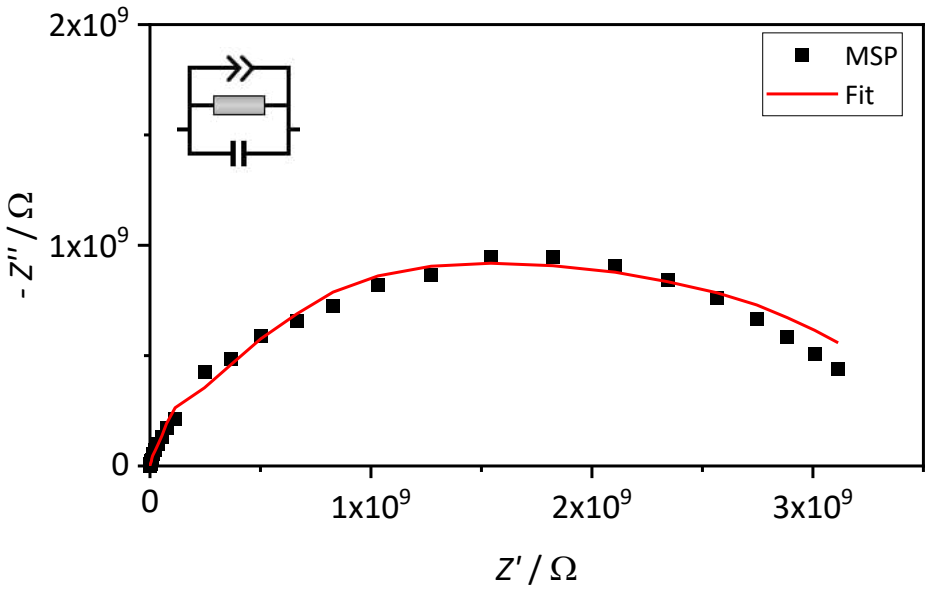

Figure 12 Nyquist plot of MSP at 25 °C in the frequency range from 3 MHz to 100 mHz together with the fit and the equivalent circuit used for fitting.

5.2 Electrochemical characterizations of QSE

5.2.1 Ratio Optimization

Since the pure MSP only has such poor conductivity and high porosity, it shall be tested if ionic conductivity can be improved by forming a QSE by combining MSP with ionic liquids. The ionic conductivity of QSE should ideally be high enough for Mg^{2+} to migrate and to plate and strip at Mg metal anodes at moderate temperatures, ideally at room temperature. Moreover, the IL content should be high enough to cover the surfaces of

the SE particles and decrease the resistance at the SE particle boundaries and the electrolyte-electrode interfaces. In addition, the QSE is supposed to maintain its solid appearance. SE-ionic liquid electrolyte mixtures with three different weight ratios are investigated. Their room temperature conductivity and the activation energy (E_a) for conduction are determined for a first look at the performance and to investigate the influence of the ratio used when combining the solid electrolyte MSP and the ionic liquid electrolyte (EMIM TFSI and PYR14TFSI). As introduced before, the QSEs are summarized in the following Table 5.

Table 5 Summary list of prepared QSE with EMIM TFSI and PYR14 TFSI ionic liquid electrolytes.

QSE abbreviation	Solid electrolyte	Mg salt	Ionic liquid cation	Ionic liquid anion	Weight ratio MSP:IL
EMIM TFSI 9:1	MSP	1 M $Mg(TFSI)_2$	EMIM	TFSI	9:1
EMIM TFSI 8:2	MSP	1 M $Mg(TFSI)_2$	EMIM	TFSI	8:2
EMIM TFSI 7:3	MSP	1 M $Mg(TFSI)_2$	EMIM	TFSI	7:3
PYR14 TFSI 9:1	MSP	1 M $Mg(TFSI)_2$	PYR_{14}	TFSI	9:1
PYR14 TFSI 8:2	MSP	1 M $Mg(TFSI)_2$	PYR_{14}	TFSI	8:2
PYR14 TFSI 7:3	MSP	1 M $Mg(TFSI)_2$	PYR_{14}	TFSI	7:3

The prepared QSEs showed conductivities at 25 °C between 10^{-6} to 10^{-4} S cm^{-1}, summarized in Table 6, together with the determined activation energies. Overall, the conductivity is greatly improved compared to pure MSP. The EMIM and PYR14 cation's respective weight ratios have comparable ionic conductivities in the same order of magnitude. Increasing the weight ratio of the ionic liquid increases the determined conductivity by one order of magnitude in each case. The E_a of the QSEs are very similar at about 550 meV, and no ratio has a noticeable lower E_a. The E_a is the same, considering the uncertainty of measurement.

Table 6 Room temperature conductivity (25 °C) and E_a of the different QSEs.

Quasi-solid electrolyte	σ(25°C)/ S·cm^{-1}	E_a / eV
EMIM TFSI 9:1	$3.9 \cdot 10^{-6}$	0.52 ± 0.02
EMIM TFSI 8:2	$6.7 \cdot 10^{-5}$	0.57 ± 0.02
EMIM TFSI 7:3	$3.4 \cdot 10^{-4}$	0.59 ± 0.03
PYR14 TFSI 9:1	$5.5 \cdot 10^{-6}$	0.57 ± 0.02
PYR14 TFSI 8:2	$3.9 \cdot 10^{-5}$	0.53 ± 0.02
PYR14 TFSI 7:3	$2.4 \cdot 10^{-4}$	0.52 ± 0.02

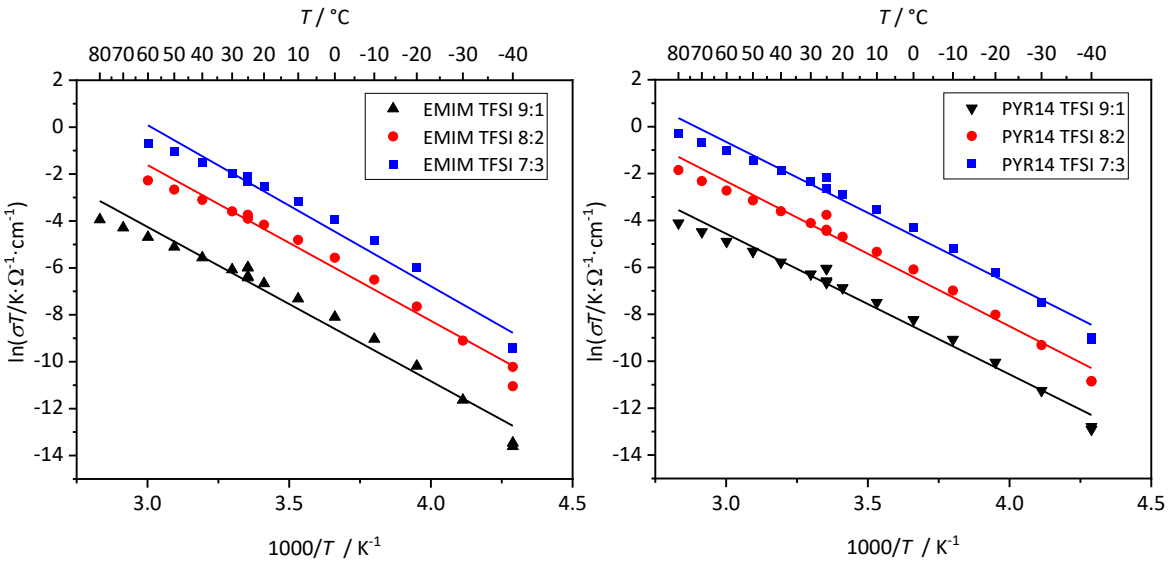

Figure 13 Arrhenius plots showing the temperature dependent conductivity of different QSEs.

The impedance measurements from the QSEs at 25 °C before, during, and after the temperature cycle for E_a measurements show a small deviation. The determined conductivity for the QSE before and after the temperature cycle differs slightly. Visibly in the ln(σT) vs. 1000/T plots, shown in Figure 13, the values at 25 °C do not match exactly. As well, the values do not show a perfectly straight line. To exclude the possibility that the measurement was performed in a not wholly equilibrated state. Two measurements were repeated by increasing the time to let the system equilibrate at the set temperature from 1.5 h to 3 h. The Arrhenius plots are given in the appendix in Figure 45. The measurement with increased equilibration time gave the same result, which means that the deviation can not come from measurements at an unequilibrated state. The reason has to lie with the studied system. The QSE partially contains the ionic liquid component, whose viscosity depends on the temperature. The viscosity decreases

at higher temperatures and increases at lower temperatures. These changes may result in a variation of contact inside the QSE composite and the contact between the current collector and electrolyte. The impedance measurement is sensitive to changes in the contact since a decreased contact increases the measured resistivity and vice versa. It should also be remembered that the equation used to describe the temperature dependency of conductivity is derived for the case of an SE with conduction over the hopping mechanism. With the introduction of the ionic liquid, we introduce a component with a possibly different conduction mechanism. But since ionic liquid concentration is low, the deviation is not severe.

In the Nyquist representations of the measured impedance spectra, depicted in Figure 14, only a simple semicircle in the high-frequency region, entering into a steep increasing line at lower frequencies, is visible. This is a typical impedance behavior of a solid electrolyte. Only a part of the semicircle is visible in the frequency range covered by the measurement. With the frequency range of the potentiostat, only the general conductivity of the QSE can be determined. Distinguishing between bulk and grain boundary resistance is not possible. The overall conductivity is slightly higher for QSEs with EMIM cation, and the conductivity increases with the amount of ionic liquid.

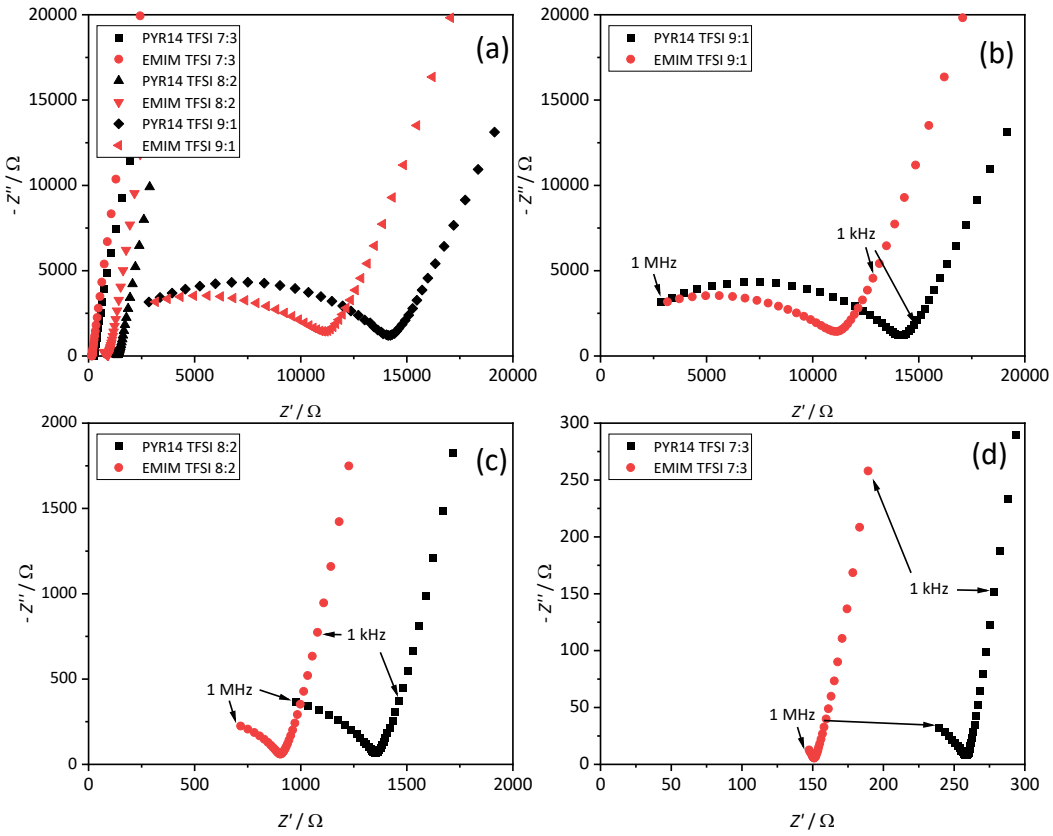

Figure 14 Nyquist plots of different PYR14 TFSI and EMIM TFSI QSE (a). Enlarged representation of the impedance spectra of ratio 9:1 (b), 8:2 (c), and 7:3 (d) recorded at room temperature with stainless steel as blocking electrodes.

The ability to allow to strip and plate Mg^{2+} from Mg metal anode at a low overpotential is also vital for a Mg electrolyte. In this case, the quality of the QSEs can be evaluated by the Mg stripping/plating redox overpotential and the stability over a long time scale. An increasing overpotential is the sign of instability, likely caused by the continuous degradation of electrolyte, with the passivation of the Mg surface at the electrode-electrolyte interface. Apart from ionic conductivity, to better evaluate the different QSEs, stripping and plating experiments in symmetrical cells are performed at a temperature of 60 °C with a current of 1 µA (current density of 1.57 µA·cm^{-1}) for 50 cycles. The corresponding potential profiles of the symmetrical cells are displayed in Figure 15 and Figure 14.

For the PYR14 TFSI QSEs, the 7:3 ratio shows the lowest overpotential yet, with an increase during cycling. At the 50th cycle, a potential of around 65 mV was observed. The 8:2 ratio showed the most stable overpotential over 50 cycles, reaching 88 mV. For

PYR14 TFSI, the 9:1 ratio shows the highest overpotential, increasing further during cycling to about 150 mV. The trend is consistent with the ionic conductivity. Namely, the overvoltage is generally lower with a higher ionic liquid content, corresponding to a lower resistance across the QSE and the QSE/electrode interface.

The overpotential for plating and stripping with the QSE containing the EMIM cation is bigger than with the PYR14 cation for all ratios over 50 cycles. For EMIM TFSI, the 7:3 ratio shows the lowest overpotential at around 100 mV, followed by the 9:1 ratio at 200 mV. Surprisingly the 8:2 ratio has the highest overpotential reaching 350 mV. But there are no notable changes in overpotential over 50 cycles. The EMIM TFSI 9:1 and 8:2 ratios demonstrate potential spices at the beginning of each cycle step indicative of a nucleation process. For the 8:2 ratio, the nucleation overpotential also remains constant over the 50 cycling procedures, suggesting a rather stable Mg redox behavior in each cycle.

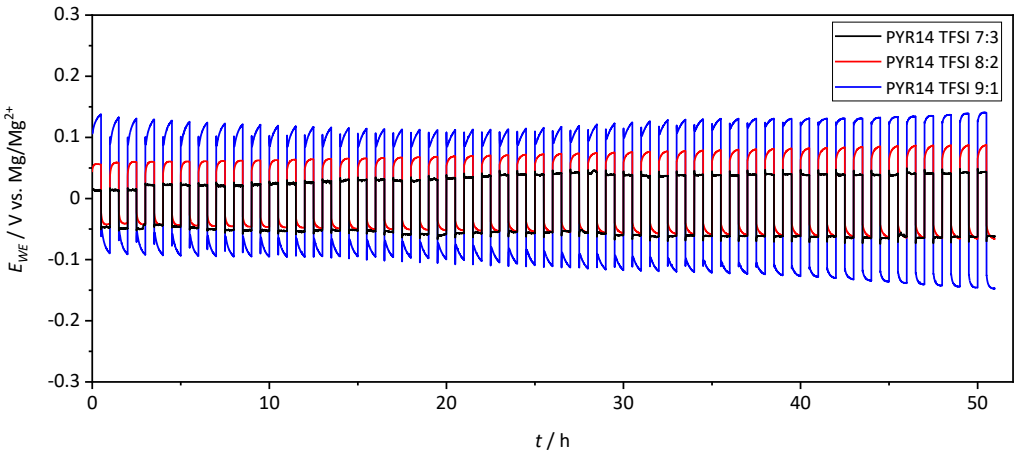

Figure 15 Potential profiles of the Mg deposition-stripping in Mg/QSE/Mgsymmetrical cells measured at 60 °C with a current density of 1.57 µA·cm^{-1} for the PYR14 TFSI QSEs of the different weight ratios.

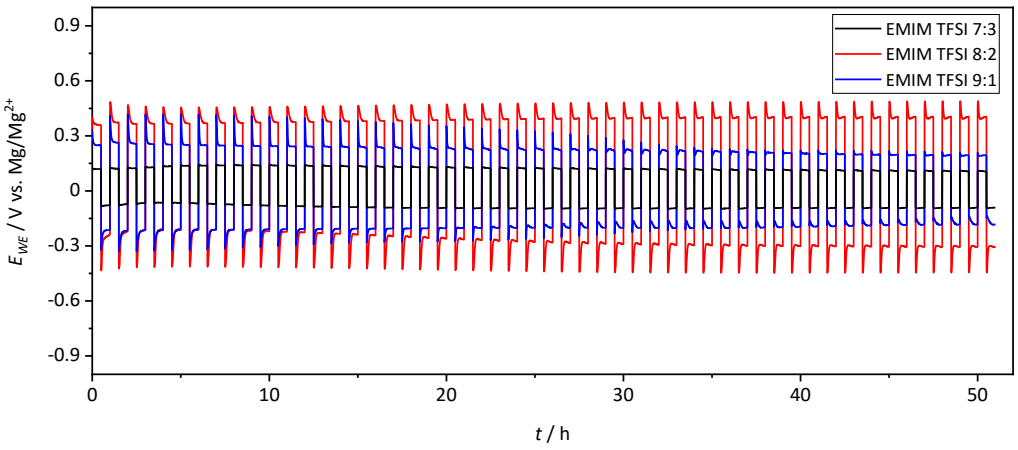

Figure 16 Potential profiles of the Mg deposition-stripping in Mg/QSE/Mgsymmetrical cells measured at 60 °C with a current density of 1.57 μA·cm⁻¹ for the EMIM TFSI QSEs of the different weight ratios.

The Mg foils of the cells were taken for ex-situ investigation with SEM and EDX. All Mg surfaces facing the QSE of the cells have traces of the SE from the QSE firmly attached to the surface, and all are covered with a seemingly homogenous distribution of the IL.

In a nutshell, for both PYR14 TFSI and EMIMTFSI, the ionic conductivities increase with the ionic liquid's content while the activation energies of all the samples are more or less the same. As for the Mg plating/stripping overvoltages in symmetrical Mg cells, both PYR14 TFSI and EMIM TFSI show stable cycling behavior in terms of overvoltage at a weight ratio of 8:2. To minimize possible influences of too many variables on the investigated system, the ratio 8:2 was chosen as a compromise to allow a comparison between the different electrolytes.

5.2.2 Chloride QSE with optimized ratio

As an alternative to the TFSI anion, a pyrrolidinium haloaluminate ionic liquid is probed for its compatibility with the studied system. The objective is to see the effect of different anions on the QSEs, such as whether switching to chloride-based anions has some advantages in the Mg transport behaviors, including increasing the conductivity of the QSE and reducing Mg plating and stripping overpotential in the symmetric cell system, etc. The $[PYR_{14}Cl/(AlCl_3)_{1.5}]$ ionic liquid is not a simple ionic liquid electrolyte. With $MgCl_2$ as conducting salt, the electrolyte has different anionic species comprised of aluminum chloride and magnesium chloride existing in an equilibrium state. In its pure form with $MgCl_2$, this ionic liquid electrolyte reportedly shows good conductivity

and a very high coulombic efficiency in the deposition and stripping of an Al/Mg alloy with a low overpotential.[7]

Following the determined weight ratio in the previous study on TFSI anions-based QSE, the chloroaluminate ionic liquid-based QSEs were also prepared with an 8:2 ratio of MSP to the ionic liquid, without and with $MgCl_2$ salt. The following Table 7 summarizes the prepared electrolytes. Again room temperature conductivity and E_a are determined, listed in Table 8, followed by the symmetrical cell experiment of stripping and plating with 1 µA (current density of 1.57 µA·cm^{-1}) for 30 min in each direction over 50 cycles at 60 °C.

Table 7 Summary list of prepared QSEs with Pyrrolidinium chloroaluminate ionic liquid.

Sample abbreviation	Solid electrolyte	Mg-conducting salt	Ionic liquid cation	Ionic liquid anion	Weight ratio MSP:IL
PYR14 Cl	$Mg_{0.5}Sn_2(PO_4)_3$	––	$PYR_{14}Cl$	1.5 $AlCl_3$	8:2
PYR14 Cl MgCl2	$Mg_{0.5}Sn_2(PO_4)_3$	0.5 M $MgCl_2$	$PYR_{14}Cl$	1.5 $AlCl_3$	8:2

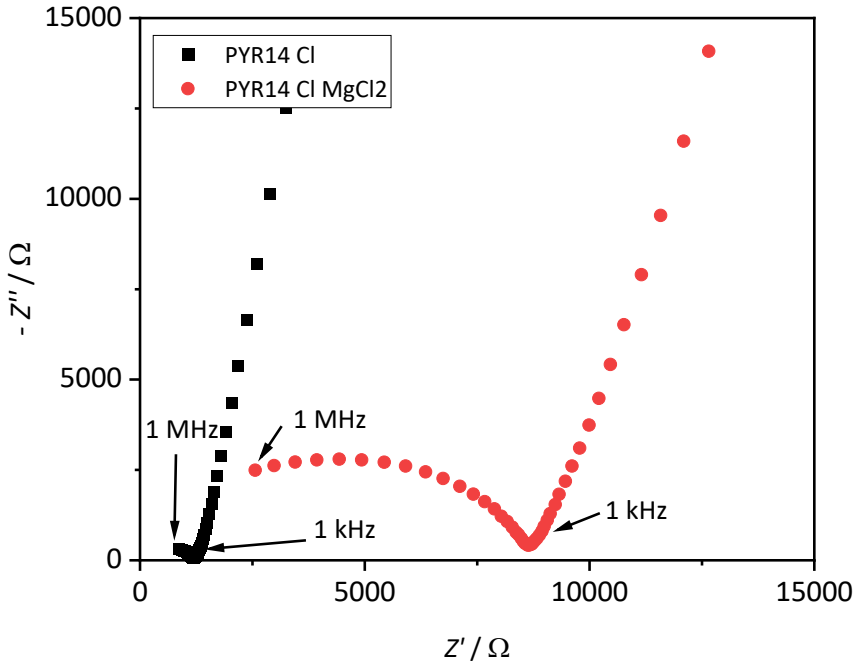

Figure 17 Nyquist plots of the [$PYR_{14}Cl/(AlCl_3)_{1.5}$] QSE without $MgCl_2$ and with 0.5 M $MgCl_2$ recorded at room temperature with stainless steel as blocking electrodes.

As shown in Table 8, although the room-temperature ionic conductivities of the QSEs with aluminum chloride are comparable to those of QSEs with TFSI anions, a much higher E_a is obtained. The E_a further increases with the addition of $MgCl_2$, leading to a higher resistance visible as the bigger semicircle in the Nyquist plot, shown in Figure 17, and thus a decrease in conductivity. The high $MgCl_2$ concentration resulted in a high viscosity of the ionic liquid electrolyte, and higher viscous liquid electrolytes have diminished conductivity.[7] It was assumed that the viscosity effect is less critical since the ion conduction occurs mainly over the SE particle in the QSE, and increasing the Mg concentration in the QSE would improve the conductivity. But apparently, the QSE works better without $MgCl_2$ addition. The symmetrical cell experiment reinforces this finding, with the potential profiles shown in Figure 19.

Table 8 Room temperature conductivity (25 °C) and E_a of the $[PYR_{14}Cl/(AlCl_3)_{1.5}]$ QSE without $MgCl_2$ and with 0.5 M $MgCl_2$.

Quasi-solid electrolyte	**σ(25°C)/ S cm^{-1}**	**E_a / eV**
PYR14 Cl	$3.69 \cdot 10^{-5}$	0.90 ± 0.01
PYR14 Cl MgCl2	$5.41 \cdot 10^{-6}$	1.20 ± 0.03

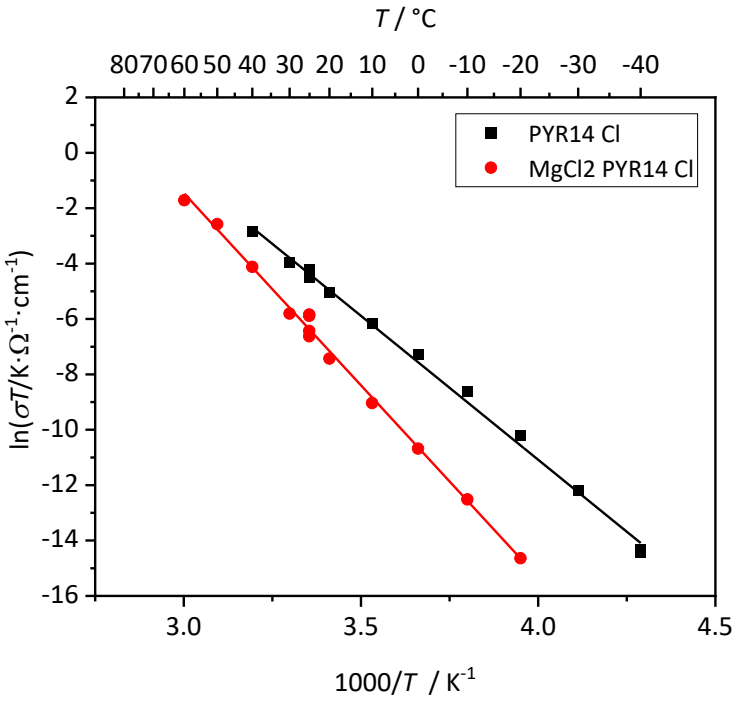

Figure 18 Arrhenius plots of the temperature-dependent conductivity used for determining the E_a of the $[PYR_{14}Cl/(AlCl_3)_{1.5}]$ QSE without $MgCl_2$ and with 0.5 M $MgCl_2$. For determinating the E_a of the QSE without $MgCl_2$, experimental values above 40 °C were ignored because of a strong deviation from linearization.

In the symmetrical cell test at 60 °C with a current of 1 µA (current density of 1.57 µA·cm^{-1}), the QSE without $MgCl_2$ appears to reach a stable overpotential of 2 V, while the one with $MgCl_2$ has a steady increase in overpotential, reaching 3.8 V at the 50th cycle. It suggests that the chloride in the QSE might passivate the Mg surfaces. The QSE without $MgCl_2$ has a lower concentration of excess chloride, which should lead to the formation of a thinner passivation film. For the QSE with $MgCl_2$, the overpotential increases progressively over time, comparable with an increasing passivation layer thickness. Additionally, corrosion is visible for the QSE with $MgCl_2$ at the stainless steel contacts where the electrolyte was in contact with the stainless steel current collector. During the cycling, the potential increased above 2.5 V, explaining the corrosion due to chloride ions.[27]

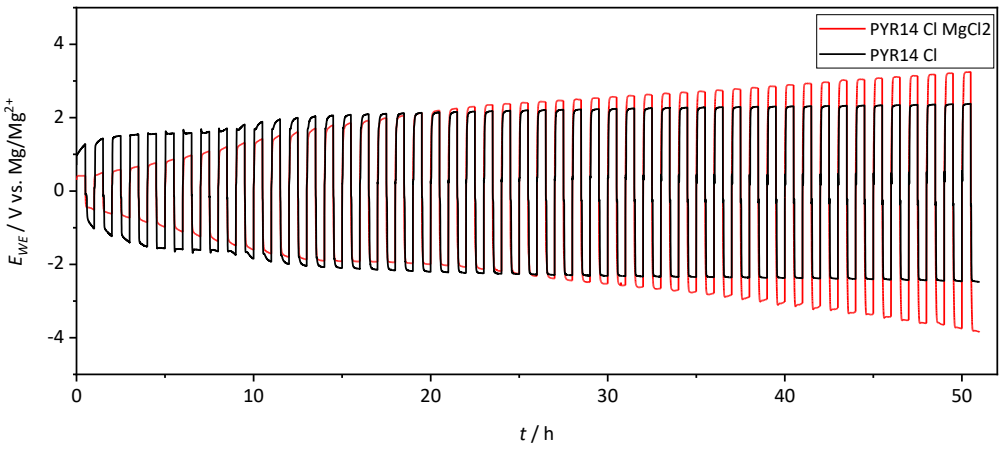

Figure 19 Potential profiles of the Mg deposition-stripping in Mg/QSE/Mgsymmetrical cells measured at 60 °C with a current density of 1.57 µA·cm^{-1} for [$PYR_{14}Cl/(AlCl_3)_{1.5}$] QSE without $MgCl_2$ and with 0.5 M $MgCl_2$.

The surface morphology of the Mg foil facing the QSE was investigated using SEM and EDX mapping after the symmetrical cell experiment at 60 °C. The cells were disassembled and prepared for analysis as described in the experimental section. EDX reveals that all Mg surfaces are seemingly homogenously covered with ionic liquid components. For the PYR14 Cl $MgCl_2$ cell, the electrolyte separated cleanly from the Mg foil. Figure 20 shows a SEM image with EDX elemental mapping images of the Mg foil from this cell. The Mg surface has almost no phosphorus or tin from the MSP, but the surface layer contains a lot of chloride, carbon, and oxygen. The chloride and carbon originate from the IL, while oxygen is a surface impurity of the used Mg foil and can also come from MSP. But combining the ex-situ information with the cycling data, it is to say

that a magnesium chloride passivating surface layer was formed on the Mg surface. This surface layer is less pronounced for the QSE without additional $MgCl_2$, thus showing a not so severe increase in overvoltage upon cycling.

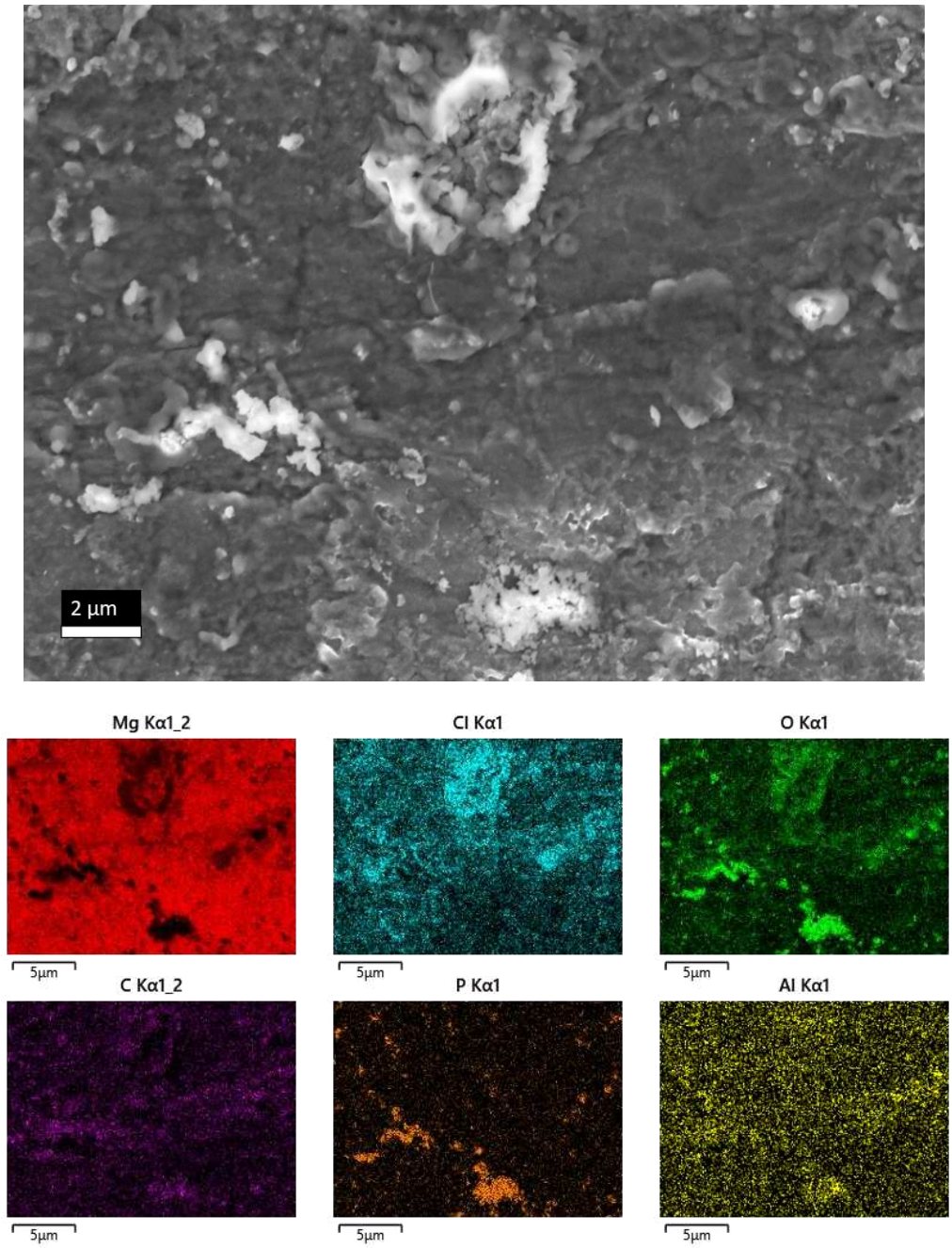

Figure 20 SEM image showing the Mg foil surface from the symmetric cell experiment with [$PYR_{14}Cl/(AlCl_3)_{1.5}$] 0.5 M $MgCl_2$ QSE at 60 °C plating and stripping experiment and related images with elemental mapping for Mg, Cl, O, C, Al, and P. This SEM picture was taken using the inlens detector. All following SEM images were taken with a secondary electron detector placed at an angle of 45° to the electron beam to get a better perception of the topology.

Above all, the overpotential of the symmetric cells is high for the aluminum chloride type QSE. Even more importantly, the interphase derived from [$PYR_{14}Cl/(AlCl_3)_{1.5}$] ionic liquid could be too complex. Since the Cl-based QSEs show inferior Mg-conducting behaviors, further work will solely focus on the QSE with TFSI anion.

5.3 QSE of 8:2 ratio with TFSI anion

In the next part, the PYR14 and EMIM TFSI QSEs in the 8:2 ratio will be closer characterized using different techniques. The studied aspects are the structure and morphology, together with the inherent stability of the QSE system by using FTIR, XRD, and SEM in combination with EDX. In addition, important electrochemical properties of electrochemical stability and electronic conductivity are investigated.

5.3.1 FTIR

To identify the chemical environment in the QSEs, the pristine TFSI QSEs of the 8:2 ratio are investigated using FTIR and compared with the spectra of the pristine MSP and the respective ionic liquid electrolytes. The FTIR spectra for PYR14 TFSI are depicted in Figure 21, and for EMIM TFSI, Figure 22. In the FTIR spectra from the QSEs, the absorption of the phosphate group belonging to MSP is clearly visible. Other absorption bands belong to the ionic liquid electrolytes.

Particularly the ionic liquid electrolytes have weak absorption bands between 3200-2800 cm^{-1} from the C-H stretching vibrations of the EMIM and PYR14 cation.[81] In the region from 1630-1550 cm^{-1}, are the C=C and C=N valence vibrations from the EMIM TFSI ionic liquid.[82] The scissoring vibration of the -CH_3 group connected with a N-atom is visible at 1460 cm^{-1}. It is more pronounced for the PYR14 than for the EMIM cation. The CH_2 vibration in the C_4H_9 group of the PYR14 cation is at 1380 cm^{-1}, and at 1340 cm^{-1} are the CH_2 twisting vibrations.[81] The fingerprint region has pronounced absorption bands ranging from about 1200 to 550 cm^{-1}.[82] In the FTIR spectra of the EMIM and PYR14 TFSI QSE of 8:2 ratio, all observable absorption bands can be attributed to the respected ionic liquid electrolyte and the pristine MSP. No apparent change in the frequency is observable. It shows that no interaction between the MSP and the ionic

liquid changes the binding properties of the functional groups observable with the IR technique in this region, indicating that the pristine hybrid system is inherently stable.

The absorption in the region between 2400-1800 cm^{-1} is most likely caused by the spectrometer, as these bands only appear with the solid samples at a seemingly random intensity and can not be attributed to a functional group of the SE or QSE. For measurement, the MSP powder and the QSE powder are pressed into a pellet with a hand pressing tool. The pressed pellets are brittle and break easily. For measurement, the pellet is only very lightly pressed onto the diamond crystal of the spectrometer optic. The density and the contact of the pellet to the crystal vary for different measurements. Additionally, the solid samples only have very low absorption values. While the ionic liquids have uniform contact with the crystal and higher absorption, leading to smoother spectra. All spectra further needed to be normalized to compare the spectra of liquid and solids.

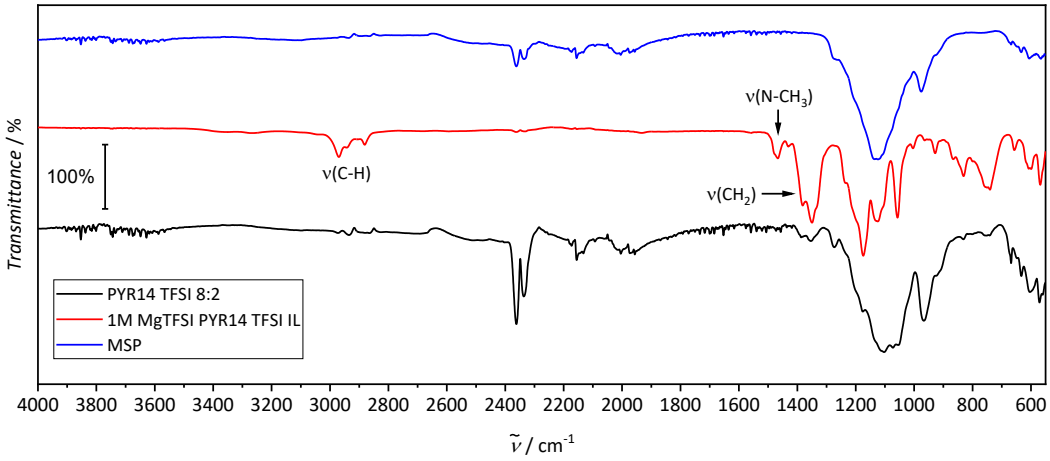

Figure 21 Comparison of normalized IR spectra of pristine MSP, ionic liquid electrolyte PYR14 TFSI, and QSE PYR14 TFSI of weight ratio 8:2.

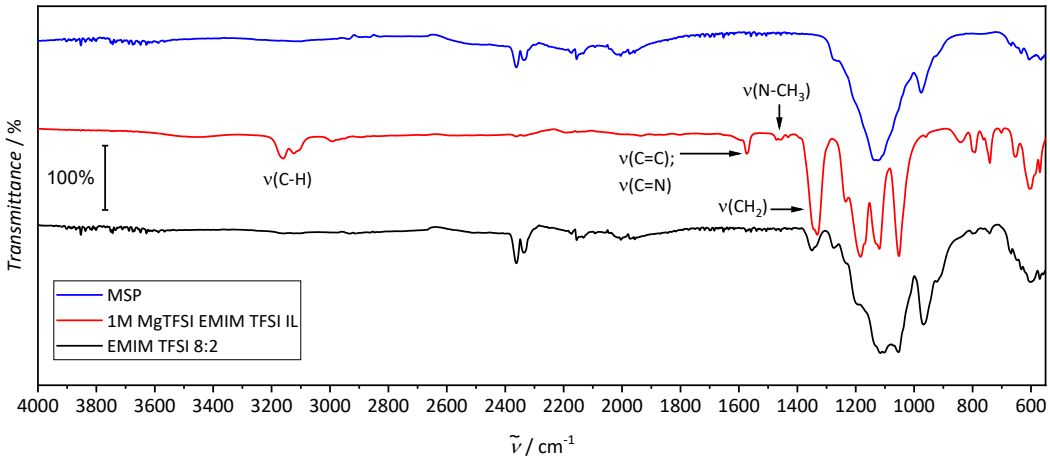

Figure 22 Comparison of normalized IR spectra of pristine MSP, ionic liquid electrolyte EMIM TFSI, and QSE EMIM TFSI of weight ratio 8:2.

5.3.2 XRD

The XRD pattern of pristine MSP and the QSEs are identical, as to see in Figure 23. The addition of ionic liquid electrolytes and the preparation method by grinding in a mortar does not influence or change the crystal structure of MSP visibly with XRD. The as-prepared QSEs are inherently stable, as shown by FTIR and XRD analysis.

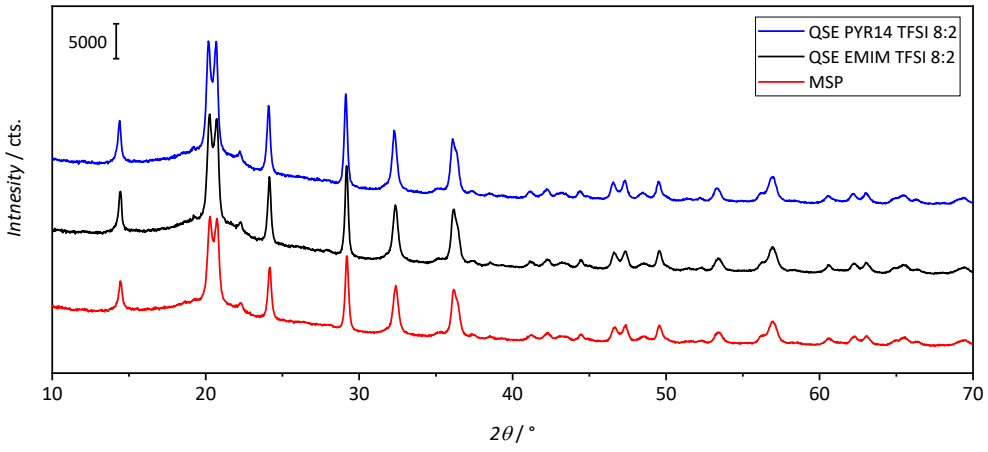

Figure 23 Comparison of powder XRD pattern from the pristine MSP powder with the QSEs of PYR14 and EMIM TFSI of 8:2 ratio.

5.3.3 SEM and EDX

The morphology of the QSE is reviewed with SEM. The addition of the ionic liquid does not visibly change the solid character of the SE, nor does it change the SE particles' morphology. The ionic liquid is not visible with the electron microscope. Like the pristine MSP, the QSEs have the same porous structure, visible in the SEM images depicted in Figure 24. Only the atomic percentages determined with EDX of the SE particles change, verifying the presence of the ionic liquid. The results of the elemental mapping with EDX are summarized in Table 9. The carbon content increases compared to pristine MSP, as well are fluorine and sulfur quantifiable with EDX. The atomic ratio of O, P, and Sn decreases to the pristine MSP, while the atomic percentage of Mg remains the same. The elemental distribution over the SE particle surface appears to be homogenous.

Table 9 Summary of results from the EDX elemental mapping. Atomic percentages for the QSE surface for EMIM and PYR14 TFSI QSE of 8:2 ratio.

	O/ Atom%	P/ Atom%	Sn/ Atom%	C/ Atom%	F/ Atom%	Mg/ Atom%	S/ Atom%
EMIM TFSI 8:2							
Average	55.9	14.4	12.7	6.7	5.8	2.6	1.9
Standard deviation	4.2	2.2	0.2	1.0	0.9	0.5	0.5
PYR14 TFSI 8:2							
Average	55.4	13.8	13.1	10.7	4.0	2.8	2.5
Standard deviation	5.3	1.5	1.2	1.1	0.6	0.4	0.1

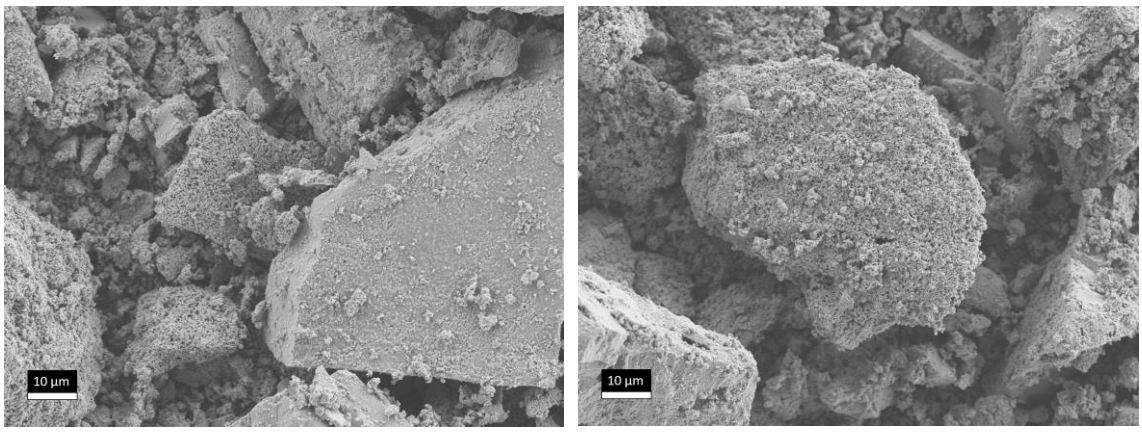

Figure 24 SEM images of the QSEs left EMIM TFSI 8:2 and right PYR14 TFSI 8:2.

5.3.4 Electronic conductivity - DC polarization experiment

Apart from high ionic partial conductivities, it is important to have no or negligible electronic conduction in an electrolyte to prevent short-circuiting. The QSE's electronic conductivity was determined over a DC polarization experiment. The calculated electronic conductivity of the QSEs is extremely low, accounting for only 0.001 % to 0.002 % of the total conductivity. With electronic conductivity being this low, the QSEs can be considered pure ionic conductors. The following Table 10 summarizes the determined electronic resistance and calculated electronic conductivities, followed by Figure 25 and Figure 26, depicting the polarization curves. In Figure 27, the graphs of the applied potential vs. the steady state current used to determine the electronic resistance over a linear fit are shown. For the set measurement time, no steady-state current was reached for the higher potentials in the DC polarization. For this reason, the electronic conductivity was determined only with experimental values between 0.1 V-1.5 V for EMIM TFSI and 0.1 V - 0.75 V for PYR14 TFSI.

Table 10 Electronic resistivity and calculated electronic conductivity from the DC polarization measurement.

Quasi-solid electrolyte	R_{el} / Ω	σ_{el} (25 °C) / S cm^{-1}
EMIM TFSI 8:2	$5.23 \cdot 10^{7} \pm 4 \cdot 10^{6}$	$1.19 \cdot 10^{-9} \pm 9 \cdot 10^{-11}$
PYR14 TFSI 8:2	$1.00 \cdot 10^{8} \pm 2 \cdot 10^{7}$	$5.96 \cdot 10^{-10} \pm 1 \cdot 10^{-10}$

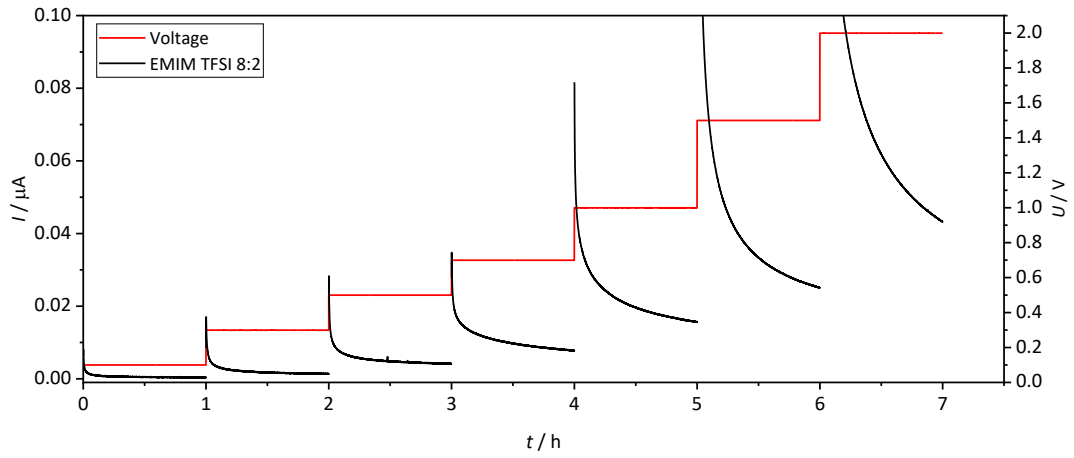

Figure 25 Current profile from DC polarization experiment for EMIM TFSI 8:2 QSE for the determination of the electronic conductivity.

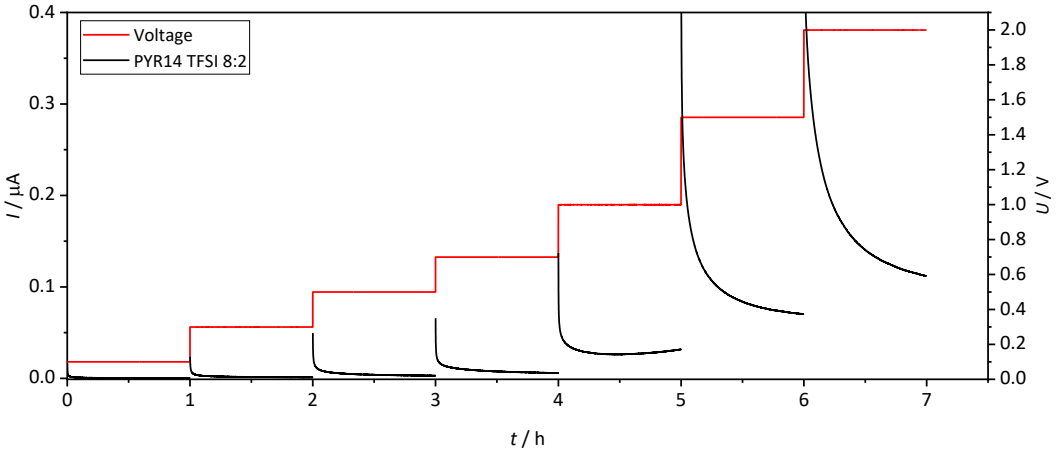

Figure 26 Current profile from DC polarization experiment for PYR14 TFSI 8:2 QSE for the determination of the electronic conductivity.

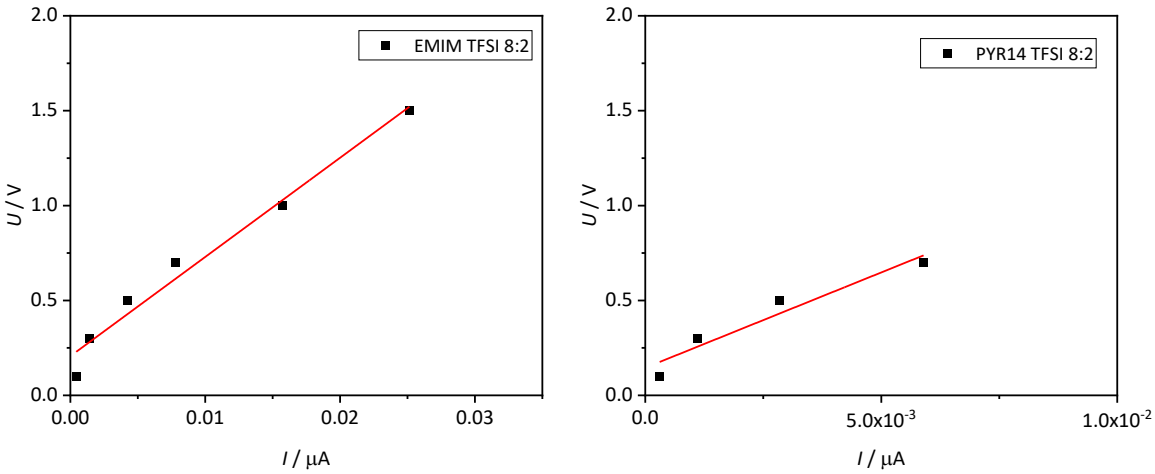

Figure 27 Potential vs. steady-state current plots used to determine the electronic conductivity at 25 °C for EMIM and PYR14 TFSI 8:2 QSE.

5.3.5 Electrochemical stability

Besides the conductivity values, another important parameter is the electrochemical stability limit of the electrolyte. An experiment to determine the electrochemical stability window was performed with stainless steel as a working electrode, Mg foil as counter and reference electrode at 25 °C. The linear sweep voltammograms are depicted in Figure 28. The electrolytes show anodic stability up to 3.69 V and 3.45 V vs. Mg/Mg^{2+} for the PYR14 TFSI 8:2 and the EMIM TFSI 8:2 QSE, respectively. These values

for oxidative stability are high, and oxidative stability over 3 V vs. Mg/Mg^{2+} is very good for a Mg electrolyte.[49] As for the cathodic sweep, PYR14 TFSI QSE shows a reduction peak at -0.49 V and EMIM TFSI at -2 V, presumably attributed to the reduction of $Mg^{2+}$to Mg^0 at the stainless steel electrode. Reduction onset is at -0.61 V for EMIM TFSI and 0.89 V for PYR14 TFSI. A second reduction peak is visible at -4 V for both electrolytes, more pronounced for PYR14 TFSI. A second feature observable for both electrolytes is a shoulder on the main reduction peak at 0.7 V for PYR14 TFSI and around -1.4 V for EMIM TFSI, possibly caused by another reduction process besides the reduction of Mg ions. It is good that the reduction peak for PYR14 TFSI is observed at a low overpotential (0.49 V vs. Mg/Mg^{2+}), but not so good that a reduction process already takes place at a potential of 1 V vs. Mg/Mg^{2+} which has to be a reduction process of the ionic liquid electrolyte. PYR14 and EMIM TFSI show similar oxidational stability but an astonishing difference in the reduction stability. The EMIM TFSI QSE seemingly has higher reduction stability and should be more stable toward the Mg metal electrode.

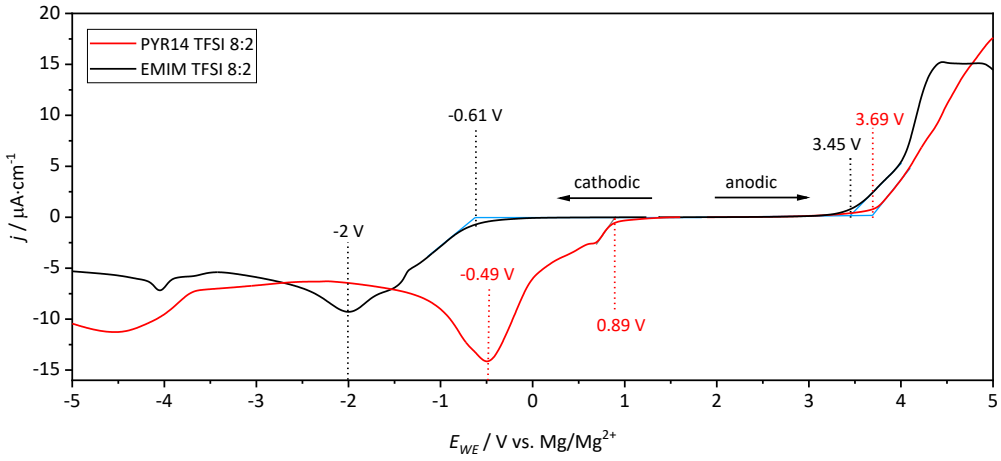

Figure 28 Profile from the linear voltammetric sweep experiment to determine the electrochemical stability limit for the EMIM and PYR14 TFSI 8:2 QSE. The linear potential sweep was performed with a scan rate of 0.1 mV s^{-1}. The arrows indicate the direction of the anodic and cathodic sweep, measured separately with different cells.

5.3.6 Symmetrical Cell- RT and 200 cycle

The cycling performance of Mg symmetrical cells was also investigated at room temperature. Potential profiles are presented in Figure 29. Here the EMIM TFSI QSE showed a stable overpotential with potential spikes at the beginning of each cycle step

like in the symmetrical cell experiment at 60 °C. The overpotential is stable over the tested 50 cycles with around 800 mV due to the decreased ionic conductivity compared to 60 °C. For PYR14 TFSI, the cycling overpotential starts at 300 mV but steadily increases and reaches 1 V at the 50th cycle. An increasing overpotential in the symmetrical cell experiment is likely caused by a progressive build-up of a passivation layer on the Mg metal surface. Since the potential does not exceed the oxidative stability limit of the electrolyte, the deterioration must come from the reduction process. This overpotential behavior confirms the higher reduction stability of EMIM TFSI compared to PYR14 TFSI.

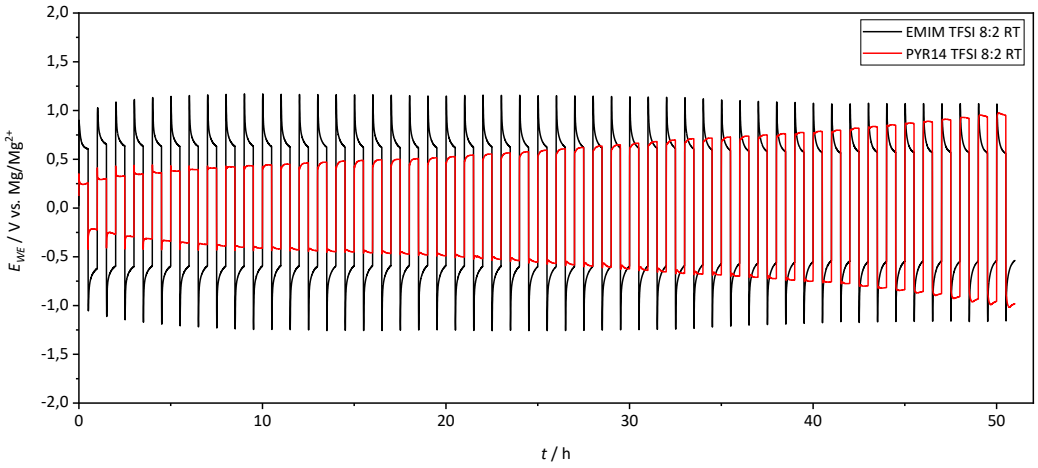

Figure 29 Potential profiles of the Mg deposition-stripping in Mg/QSE/Mgsymmetrical cells measured at room temperature with a current density of 1.57 µA·cm^{-1} for EMIM and PYR14 TFSI 8:2.

Since the QSEs of the 8:2 ratio were performing well enough in the 50 cycles of the symmetrical cell test at 60 °C, long cycling performance is tested using a current density of 7.86 µA·cm^{-1} (5 µA) at the same temperature. Figure 30 shows the potential profile of all 200 cycles together with the enlargement of three areas. Again the EMIM TFSI QSE shows higher overpotential at first than the PYR14 TFSI QSE with 450 mV but better cycling stability. Both QSEs, have a noteworthy overpotential increase after about 100 h for PYR14 and 120 h for EMIM at cycling under the used conditions, suggesting a severe degradation during long-term cycling, which still needs further study for optimization. Even so, EMIM TFSI ends up at an overpotential of 2.3 V and PYR14 TFSI at 3.4 V after cycling for 200 cycles, again confirming the higher reduction stability of the EMIM TFSI QSE.

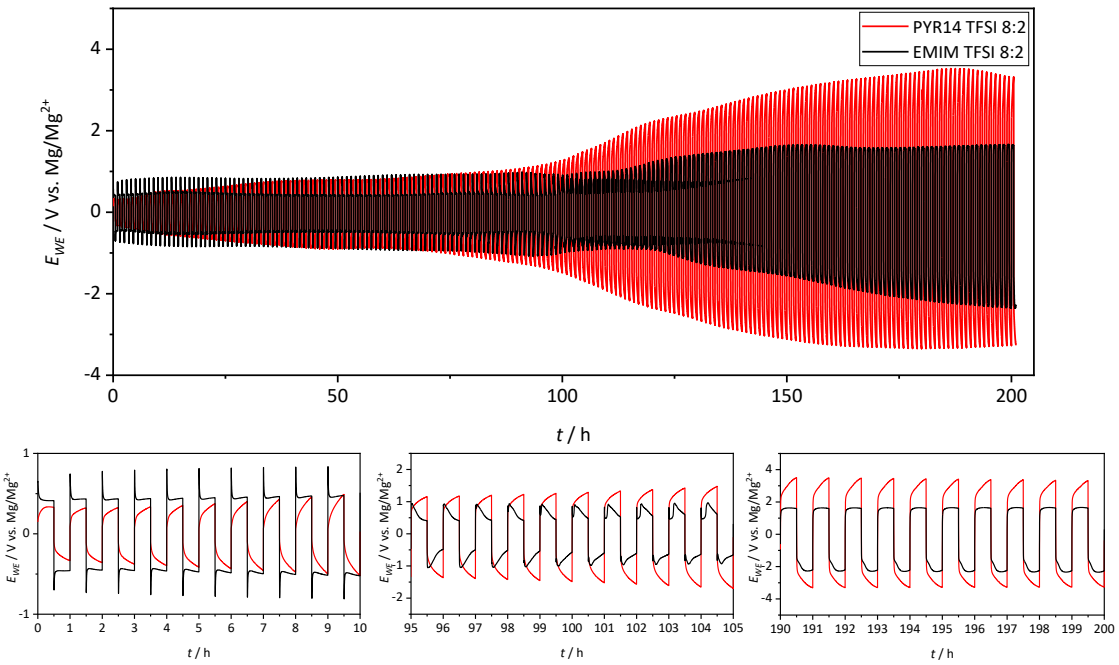

Figure 30 Potential profiles of the Mg deposition-stripping in Mg/QSE/Mgsymmetrical cells measured at room temperature with a current density of 7.86 µA·cm^{-1} for EMIM and PYR14 TFSI 8:2.

After disassembling the cells for the EMIM TFSI QSE cell, on one side of the electrolyte pellet, shiny metallic dots are visible. These spots were also visible on the Mg foil of this side and could be attributed to the remaining deposits. The SEM pictures of the Mg foils of the cells show that they are covered with electrolytes. For the EMIM TFSI cell, a part of the Mg foil with one of the spots was chosen for SEM analysis, see Figure 31. On this foil, an area with bare Mg could be found, with the rest of the surface covered with electrolyte. This spot could be the remaining Mg deposit, and the sharp-edged morphology suggests crystalline Mg deposition.

Both QSEs seem to have problems regarding cycling stability over a prolonged time. Using an elevated temperature of 60 °C and a higher current density of 7.86 µA·cm^{-1} accelerated destructive processes, leading to Mg surface passivation, which increases the overpotential of the symmetrical cell. Surface passivation is more severe for the PYR14 TFSI QSE, while the EMIM TFSI QSE shows the dendrite formation. It should be noted that more attention needs to be paid to the interface between the QSEs and the Mg. The used cation seems to have a strong influence on the stability of the QSE with

Mg. The determined electrochemical stability for the PYR14 and EMIM TFSI QSE are similar and can thus not explain the different stability upon cycling. The key to understanding the stability might be the interaction of the cations with the TFSI anion and the used $Mg(TFSI)_2$ conducting salt. Since the degree of solvation of the TFSI anion can influence the readiness for decomposition at the metal surface.[83]

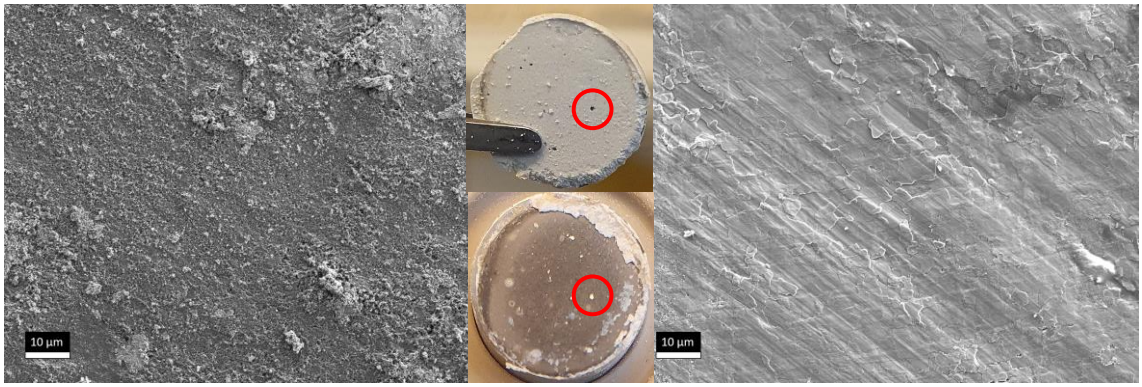

Figure 31 SEM pictures oft he Mg foil of the EMIM TFSI 8:2 symmetric cell. Left picture Mg surface covered with electrolyte. Right, Mg foil of bare Mg surface with spots of the possible remaining deposit. In the middle, pictures of the EMIM TFSI 8:2 QSE (pellet diameter 10 mm) and Mg foil (diameter 9 mm) showing the side with the remaining deposit, marked with a red circle.

5.3.7 Mg Plating Experiments

It could already be determined that the conductivity of the QSEs is ionic. But to further prove that Mg ions are conducted, it is attempted to plate Mg on an Al substrate to observe it more clearly. Since the QSE showed high enough ionic conductivity in the impedance measurement, and the symmetrical cell experiment showed acceptable overpotential at room temperature. Plating at room temperature is tried.

Asymmetric cells with the 8:2 ratio QSEs were built. An aluminum foil was used as the current collector and substrate for the Mg deposition. For the plating, a constant current of 1 µA was applied for 284 h. The resulting potential profile, in Figure 32, for the plating of the EMIM TFSI QSE shows a stable plateau at -700 mV vs. Mg/Mg^{2+} at first, which starts to increase after about 200 h. The plating for the PYR TFSI QSE starts to proceed at a comparable potential but then increases to about -1.8 V, where it stays constant. The plating experiment was followed by an ex-situ investigation of the Al foil and the QSE pellet.

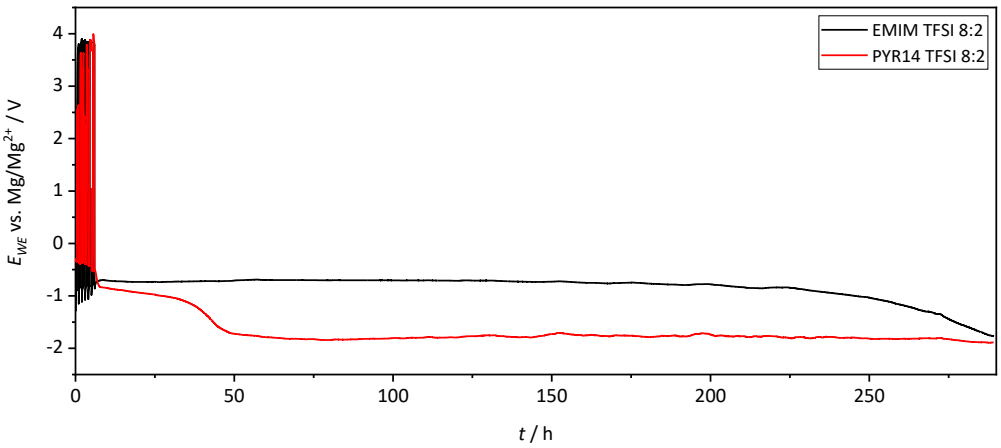

Figure 32 Voltage profile from the Mg plating experiment at room temperature using Al foil and a constant current of 1 µA.

After disassembling the cell, XRD patterns were recorded from the Al foil facing the QSE to check for crystalline Mg deposition. They are displayed in Figure 33 and Figure 34. The (011) reflex has the largest intensity for crystallin Mg at a 2θ angle of 36.6°. It could not be observed in the XRD pattern of the Al foil nor in the XRD from the QSE pellets. Both sides of the QSE pellets were investigated with XRD. There was no difference between the sides. The pattern of the QSE is the same as for the pristine MSP powder indicating that the crystal structure of the MSP is stable in the MSP at least under the conditions applied for the plating at RT. In the Al foil XRD pattern, the (111) reflex at 38.5° and the (002) reflex at 44.7° of Al are visible together with residual electrolyte.

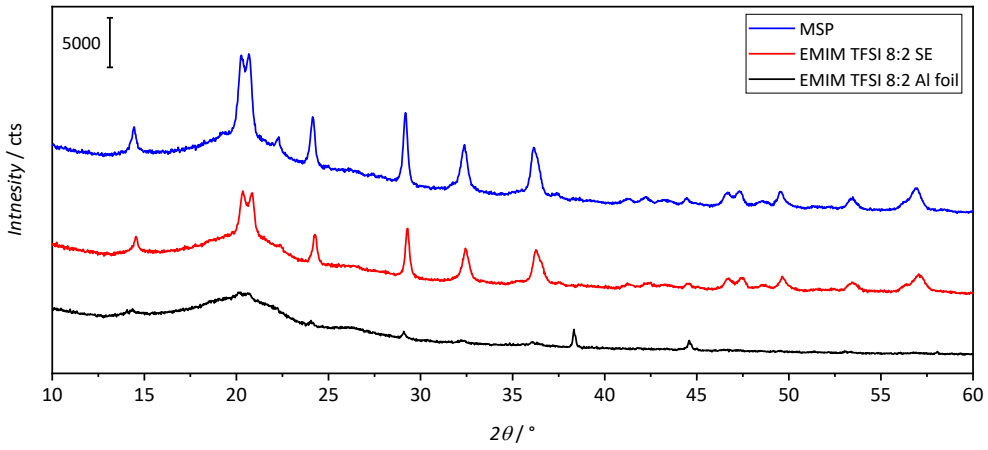

Figure 33 Comparison of XRD pattern from the Al foil and the used QSE pellet of the EMIM TFSI 8:2 cell from the Mg plating experiment at room temperature and pristine MSP powder.

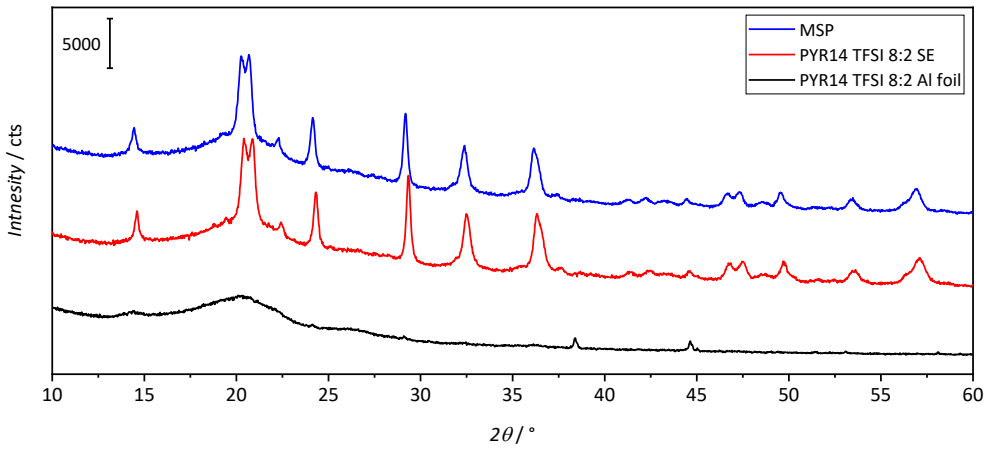

Figure 34 Comparison of XRD pattern from the Al foil and the used QSE pellet of the PYR14 TFSI 8:2 cell from the Mg plating experiment at room temperature and pristine MSP powder.

Like with XRD, no Mg deposition is visible with SEM and the EDX elemental mapping of the Al foil surface. SE residuals from the QSE cover the surfaces. Elemental mapping shows a seemingly homogenous ionic liquid layer indicating a good contact between QSE and metal foil. In the SEM images are some darker areas visible. See Figure 35 and Figure 36. These contrasting areas have structures with smooth-looking surfaces. They differentiate themselves in structure and shading from the rest of the rougher appearing surface of the aluminum foil and the SE particles. They can be found on the Al foils of the PYR14 and the EMIM TFSI cell. When EDX mapping is performed on them, it is revealed that they constitute elements found in the ionic liquid electrolyte, mainly carbon, sulfur, and fluorine, but also oxygen. They seem to be decomposition products of the ionic liquid.

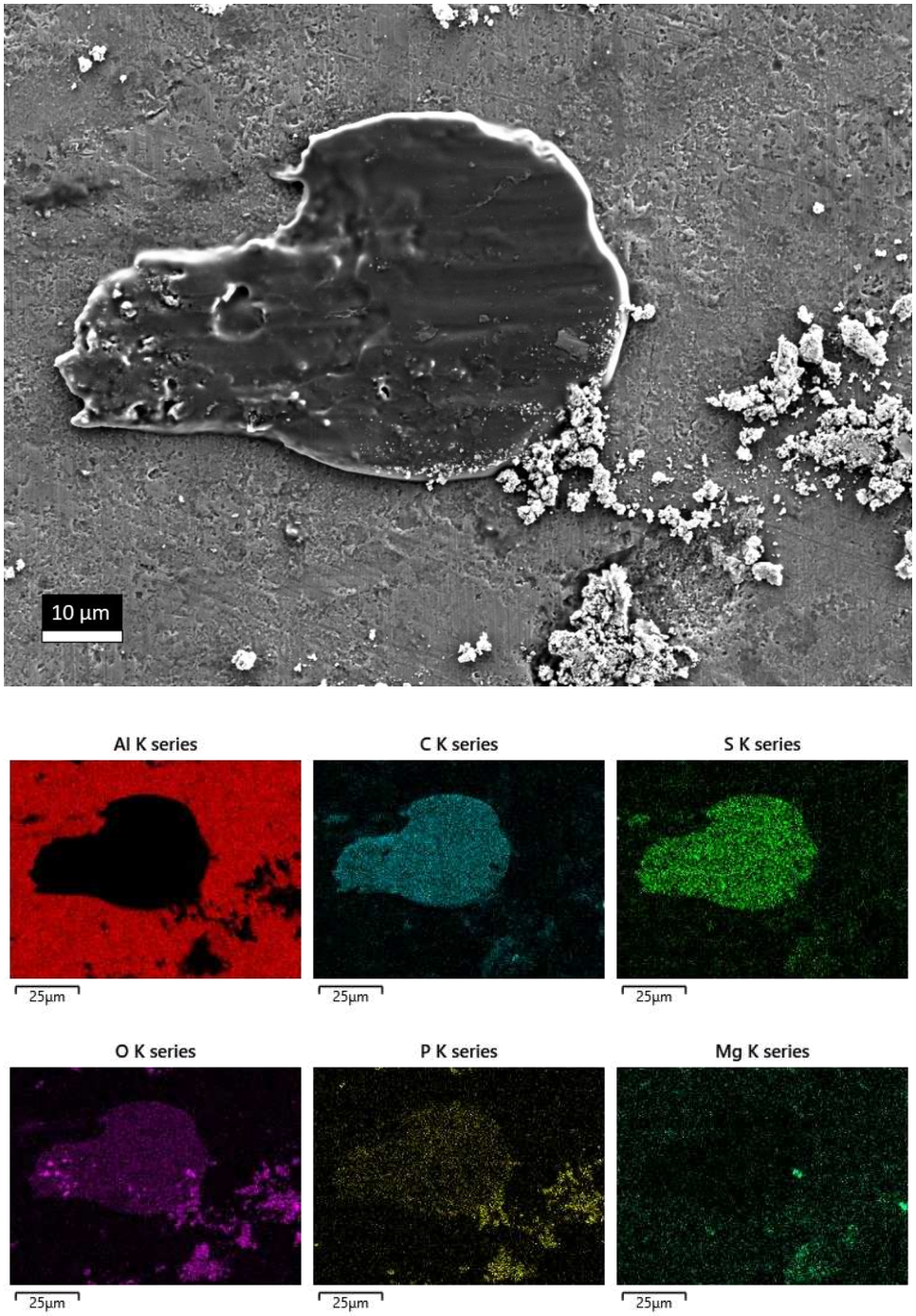

Figure 35 SEM with EDX elemental mapping images from Al foil showing the carbon-rich decomposition product from the PYR14 TFSI 8:2 cell used for the Mg plating experiment at room temperature.

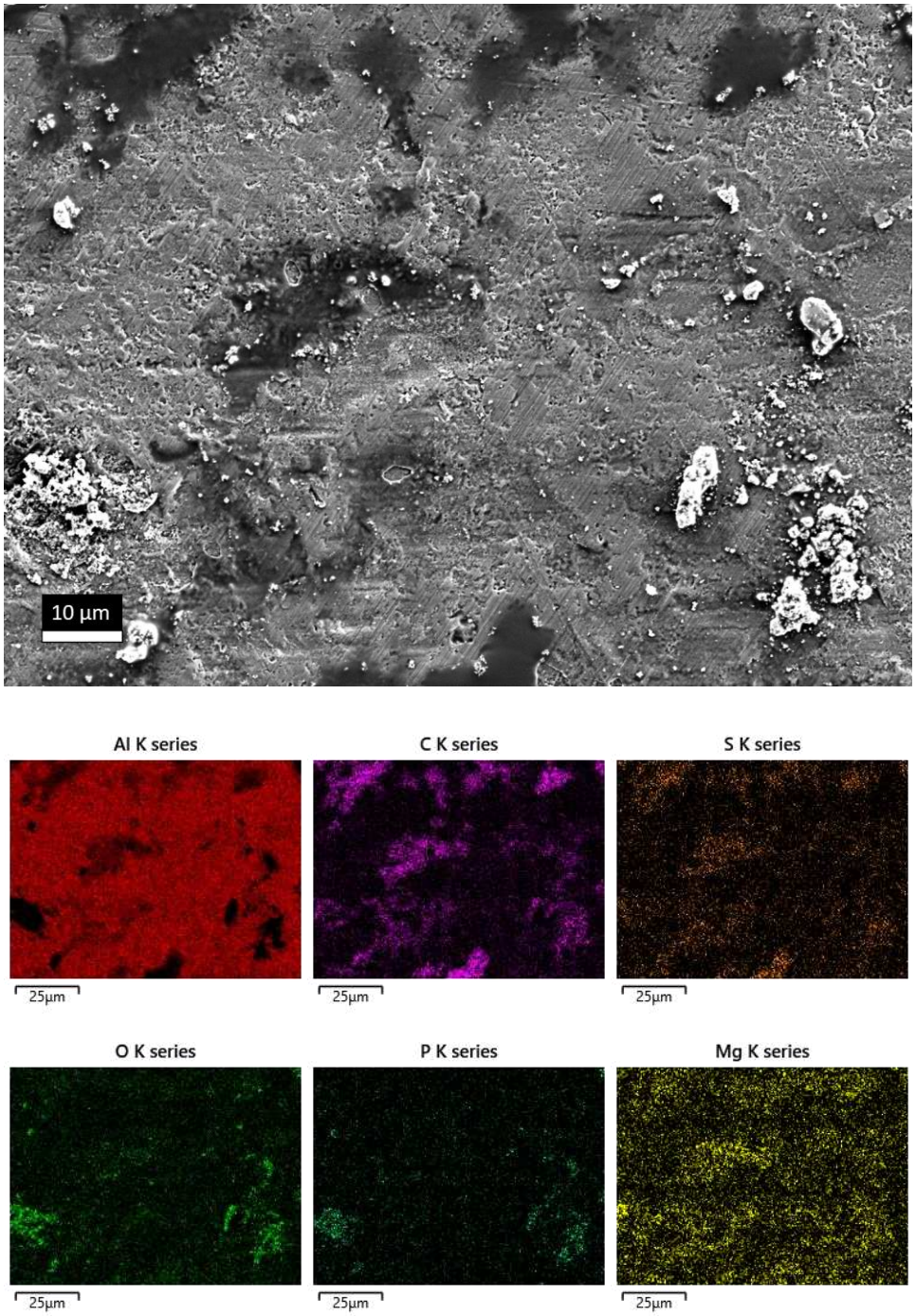

Figure 36 SEM with EDX elemental mapping images from Al foil showing the carbon-rich decomposition product from the EMIM TFSI 8:2 cell used for the Mg plating experiment at room temperature.

The standard potential of Al E^0 is -1.66 V vs. SHE, and it is very close to the standard potential of Mg of -2.36 V vs. SHE. This makes the Al foil as electrode unstable at the potentials reached during the cycling performed before the plating, leading to corrosion visible in the SEM images (Figure 37). Additionally, electron transfer currents and rates for Mg deposition on an Al electrode seem to be low compared with other electrode materials, at least for liquid electrolytes.[15]

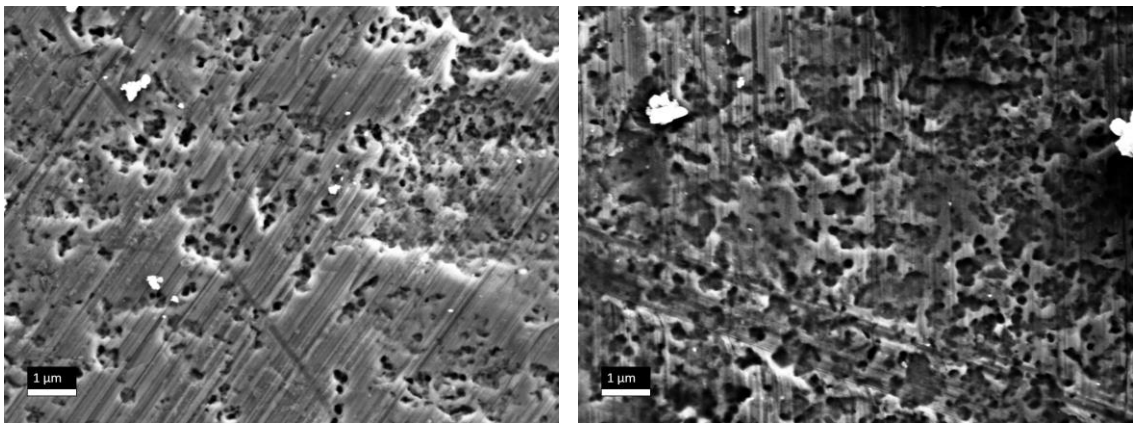

Figure 37 SEM image of the corrosion found on the Al foil of the cells using EMIM TFSI (left) and PYR14 TFSI (right) QSE.

Al foil is unsuitable as the current collector and substrate for Mg plating with the QSE, so a Cu foil was used for another attempt at Mg plating. Additionally, the temperature is elevated to 60 °C to increase the conductivity and allow the use of a higher current of 5 µA.

The plating on the Cu foil proceeds at a different potential than on the Al foil, to see in the potential profiles in Figure 38. Cu is a nobler metal than Al and has a higher standard redox potential leading to another potential difference between the electrodes and different cell potentials. On the Cu foil and at 60 °C, Mg plating proceeds between 1 V to 0.68 V for PYR14 TFSI and 35 mV to -750 mV vs. Mg/Mg^{2+} for EMIM TFSI. This time Mg is plated for only 70 h. The plating potential for the EMIM TFSI is steadily increasing after around 30 h of plating.

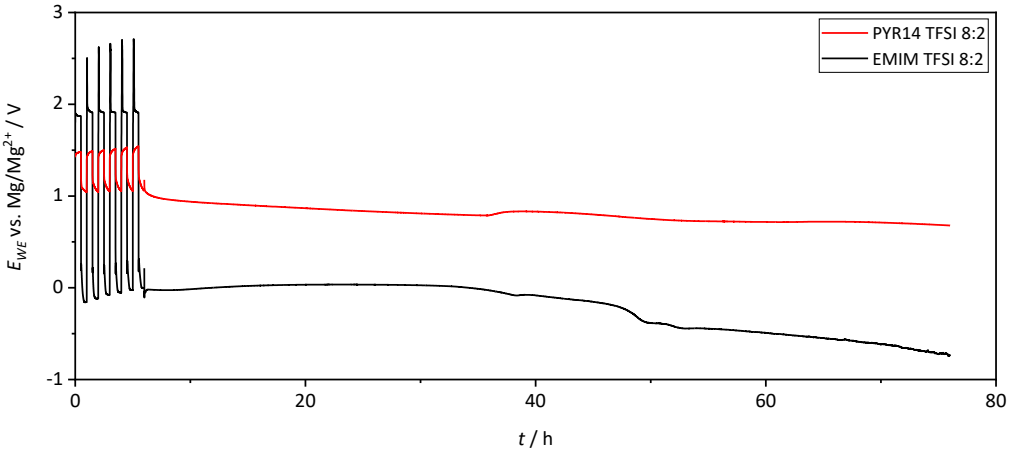

Figure 38 Voltage profile from the Mg plating experiment at 60 °C using Cu foil as plating substrate and a constant current of 5 µA.

After cell disassembling, the cell with the PYR TFSI QSE showed a greenish tint on the side of the QSE facing the Cu foil, an indication of possible reaction of the QSE with the Cu foil. The recorded XRD pattern are shown in Figure 39 and Figure 40. Again the XRD of the Cu foil showed no crystallin Mg deposition, only reflexes belonging to the Cu foil. And the XRD pattern of the two sides of the QSEs are again identical and match with the pristine MSP.

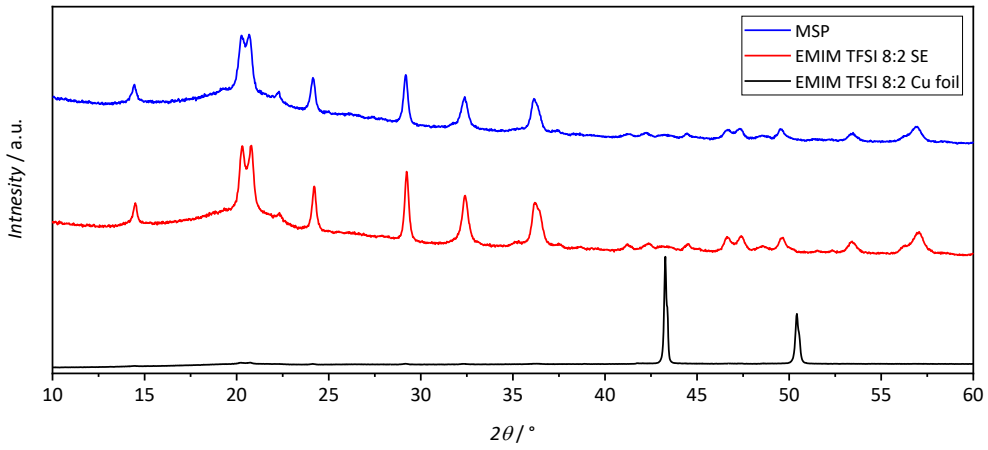

Figure 39 Comparison of XRD pattern from the Cu foil and the used QSE pellet of the EMIM TFSI 8:2 cell from the Mg plating experiment at 60 °C and pristine MSP powder.

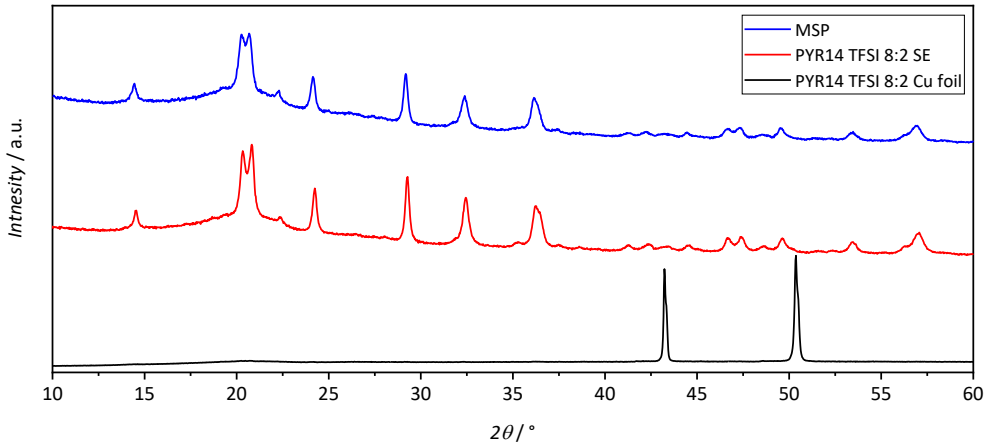

Figure 40 Comparison of XRD pattern from the Cu foil and the used QSE pellet of the PYR14 TFSI 8:2 cell from the Mg plating experiment at 60 °C and pristine MSP powder.

But with SEM and EDX mapping, Mg deposition is found on the surface of the Cu foil for both electrolytes. The deposit has a different morphology for the two electrolytes, as to see in Figure 42 and Figure 43. The deposition is spread across a larger area in the cell using the EMIM TFSI QSE. The SEM shows residuals of QSE on the Cu surface surrounded by Mg deposition with a wave-like structure. EDX reveals that the Mg is impure with the contamination of oxygen and other elements of the ionic liquid, most likely residuals from the electrolyte since the electrodes are directly taken from the cell without further cleaning.

On the Cu foil of the PYR14 TFSI cell, Mg deposition can be found in the form of small crystals in a few spots. But there are also some carbon-rich structures already found on the Al foil from the plating at RT. Despite the deposits, most of the surface for PYR14 TFSI is only covered with the QSE. For comparison, two SEM pictures from the Cu foil from the respective QSE using the same magnification are shown in Figure 41. For EMIM TFSI, the deposit is clearly visible, while for PYR14 TFSI, only the electrolyte on the surface can be recognized.

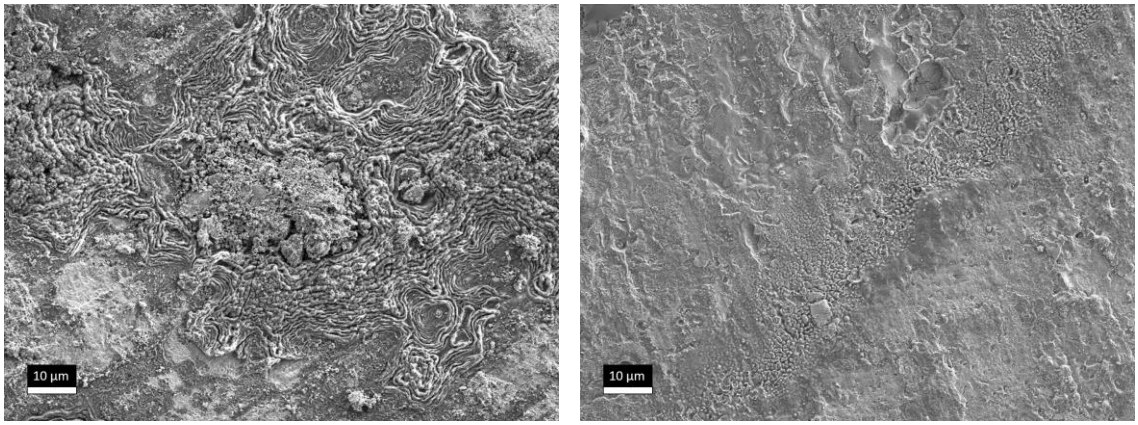

Figure 41 SEM images of the Cu foil used for Mg plating, left deposition found covering large areas of the Cu foil in the case of EMIM TFSI 8:2 QSE, and right PYR TFSI 8:2 cell Cu foil covered with QSE.

It appears that for the PYR 14 TFSI, the amount of plated Mg was too low to see an Mg reflex in the XRD, while it could be possible that the deposited Mg in the EMIM TFSI cell is amorphous considering the unusual structure.[84] The increasing plating potential for EMIM TFSI could originate from the morphology of the observed deposition. Since the Mg deposition in this cell is found covering larger areas of the Cu electrode surface. The potential of plating is probably increasing as the bare Cu surface is completely covered with a layer of Mg deposit. Lastly, since Mg plating could be confirmed, this proves that the QSE can conduct Mg ions. For EMIM TFSI QSE, a significantly larger amount of deposition could be observed due to the higher reduction stability.

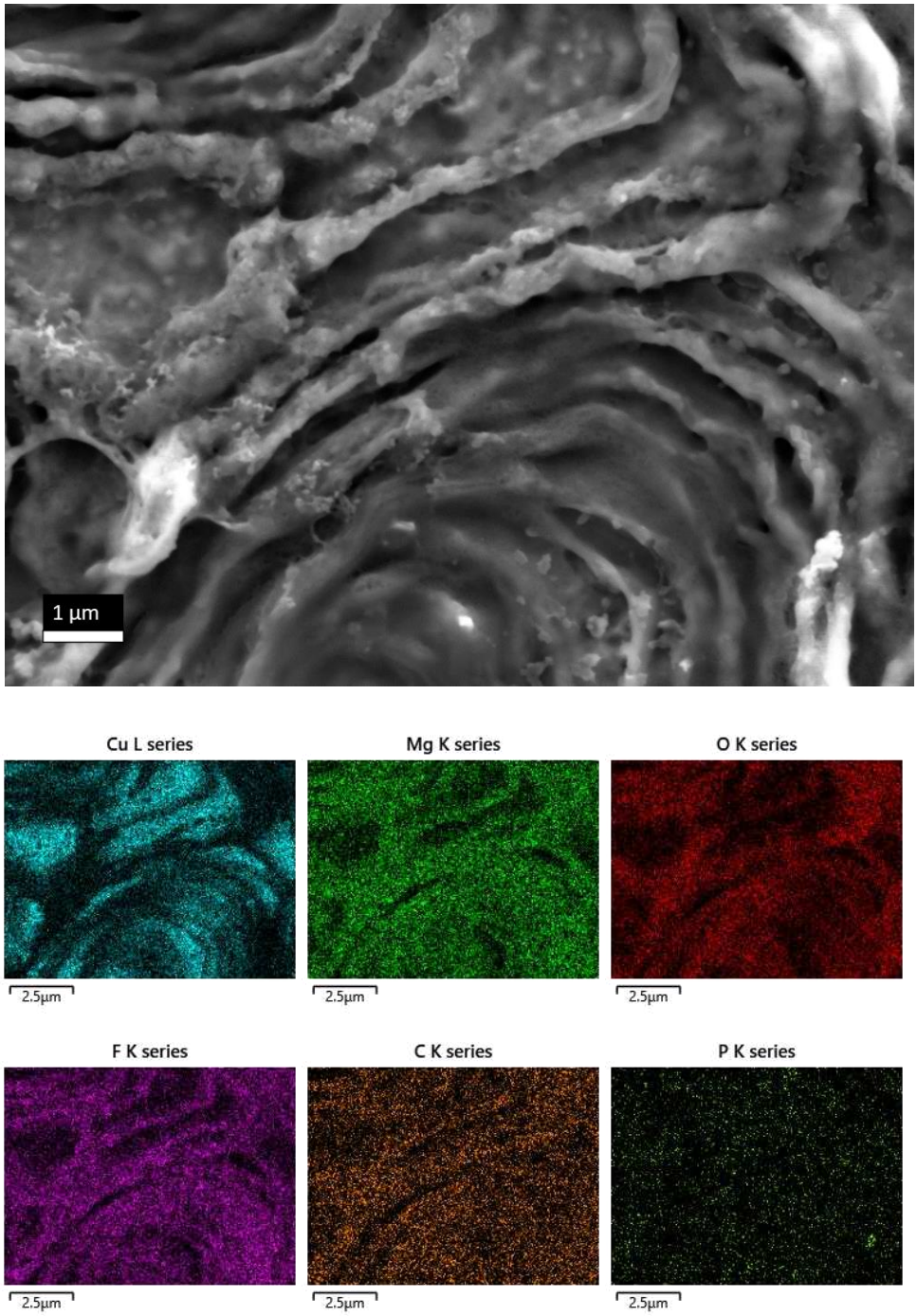

Figure 42 SEM image of Mg deposited on Cu foil for EMIM TFSI 8:2 QSE together with images of the elemental mapping from EDX.

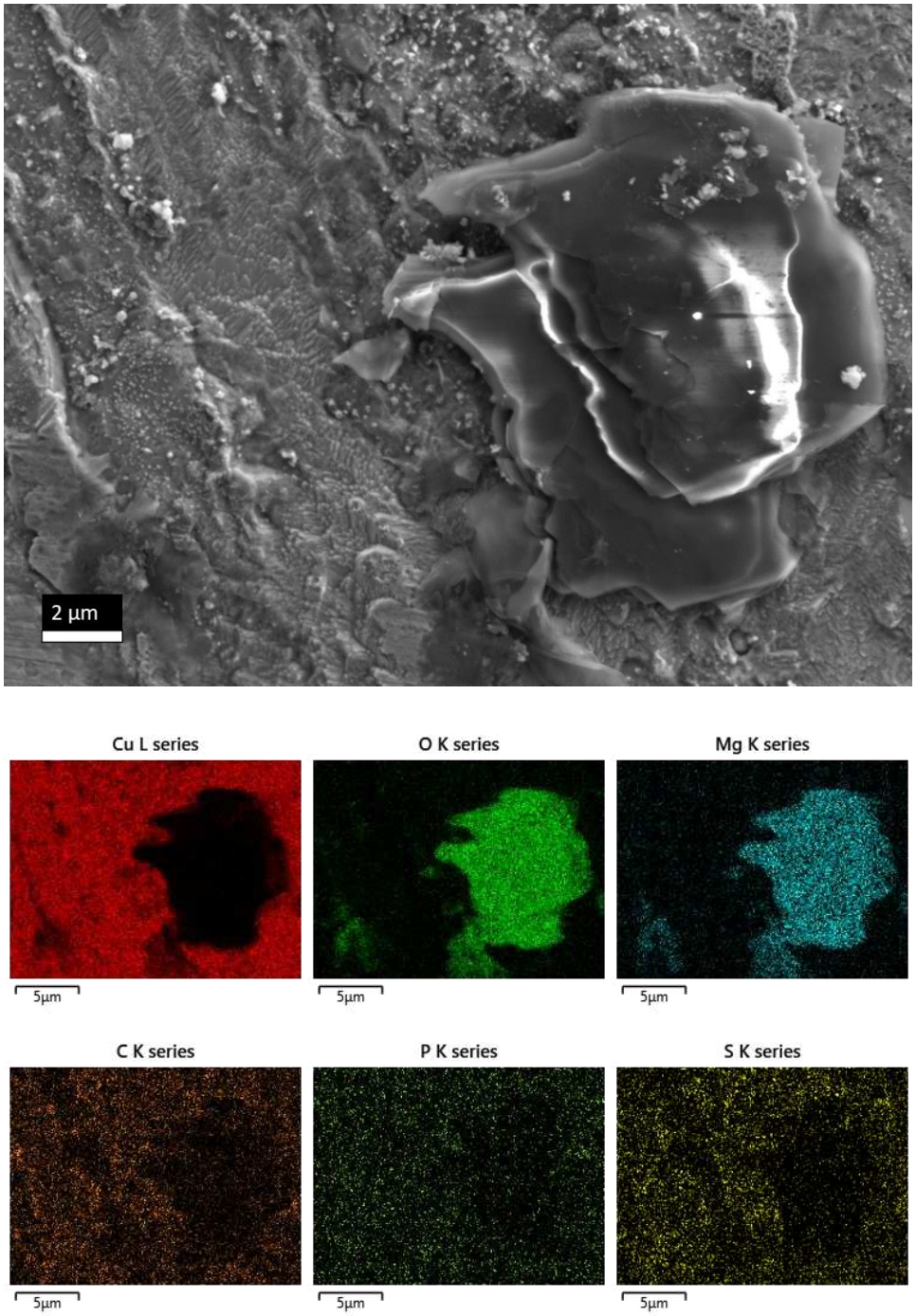

Figure 43 SEM image of Mg deposited on Cu foil for PYR14 TFSI 8:2 QSE and images of the elemental mapping from EDX.

6 Conclusion & Outlook

Adding ionic liquids to MSP can greatly improve the poor conductivity of pure MSP. The higher the ionic liquid ratio, the higher the conductivity of the QSEs was for the investigated weight ratios. An addition of 20 wt% ionic liquid electrolytes raises the conductivity enough (10^{-4} S·cm^{-1}) to allow Mg plating (60 °C and a current density of 7.86 µA·cm^{-1}), verifying Mg^{2+} conductivity. The ionic liquid seems to be well distributed on the SE particle and ensures good contact between electrodes and the QSE pellet. The crystal structure of MSP is not affected by the electrolyte, and the ionic liquid also seems to be stable with MSP. It does not change the morphology visibly in SEM, with the QSE remaining porous. Further densification should be able to improve the conductivity. It would be good to determine the porosity of the electrolytes to establish a correlation between density and ionic conductivity. Also, the thickness of the ionic liquid layer surrounding the SE particles should be determined to assess how much the higher weight ratio changes the ionic liquid layer and how the layer thickness correlates with the conductivity.

The [$PYR_{14}Cl/(AlCl_3)_{1.5}$] ionic liquid electrolyte also improved the conductivity of MSP, even without $MgCl_2$. Adding 0.5 M $MgCl_2$ to the ionic liquid in the QSE passivates the Mg metal surface and reduces the conductivity. Further, Cl^- is still problematic due to the corrosion of stainless steel electrodes above 2.5 V vs. Mg/Mg^{2+} and the MSP-[$PYR_{14}Cl/(AlCl_3)_{1.5}$]-$MgCl_2$ QSE is too complex for a model system.

The EMIM TFSI and PYR14 TFSI QSE have similar high oxidative (>3 V vs. Mg/Mg^{2+}) but different reduction stability. Since EMIM TFSI has significantly higher reduction stability than PYR14 TFSI, it is more stable in contact with Mg metal. It shows better cycling stability in the symmetrical cell experiment and a better result for Mg plating. It needs to be further investigated if solely the cation is responsible for the higher reduction stability or if the different interactions of EMIM and PYR14 with the TFSI anion[83] give rise to higher reduction stability. Experimental methods for investigation would be possible by a closer analysis of the QSE-Mg interface, including the identification of decomposition products formed at the Mg-electrolyte interface, for example, by using X-ray photoelectron spectroscopy or secondary ion mass spectrometry analysis.

Another approach would be the substitution of the TFSI anion with another simple anion. The TFSI anion works well with Li^+ since the passivation layer formed is penetrable for Li^+. With Mg, it is not analog since Li and Mg exhibit fundamentally different behavior in ion conductors due to the high charge density and the varying degrees of covalent and ionic bond character.[23] It would be interesting to test more reduction stable anions, for example, with boron, since boron-containing liquid electrolytes showed promising results for Mg deposition-stripping.

Only an obvious conductivity improvement could be verified upon adding the ionic liquid to the SE. It is still unknown over which route conduction occurs in the QSE. If shared over grain boundary and bulk or mainly over the grain boundaries at the interface of ionic liquid and SE. Since the QSE showed a slight deviation from the linearization for the activation energy, it is concluded that the ionic liquid plays a role in the conduction mechanism.

Altogether, the conductivity improvement in oxide Mg-SE by using ionic liquids looks promising. But the QSEs still need further study and an improvement in their stability to be used with pure Mg. In addition, it has not yet been investigated which cathode materials are usable with the electrolytes. This is important because a solid-state Mg battery will only work if suitable materials for the anode, electrolyte, and cathode are combined.

7 Appendix

7.1 $MgCl_2$

The XRD pattern of the pristine anhydrous $MgCl_2$, presented in Figure 44, shows sharp reflexes as expected for the crystallin starting material. To increase the solubility in the ionic liquid [85], the $MgCl_2$ is ball milled under an argon atmosphere. Zirconia oxide milling cups and balls in sizes 5 mm and 10 mm were used. In the first milling step, a rotation speed of 300 rpm for a total duration of 10 h with 10 min of milling followed by a pause of 10 min with a weight ratio of 15:1 of balls to $MgCl_2$ was used. After milling, the XRD pattern was recorded. The powder XRD pattern shows an increased intensity of the reflexes due to the reduction in particle size leading to an increased number of crystals in the sample, but no change in crystal structure was observed. For this reason, a second ball milling was performed with a total milling time of 10 h with intervals of milling at 500 rpm for 10 min, followed by a pause of 10 min. The weight ratio of balls to $MgCl_2$ used was 20:1. In the XRD, a broadening of $MgCl_2$ reflexes was observed. The reflexes broadened due to further crystal size reduction and disordering of the crystal structure.[86]

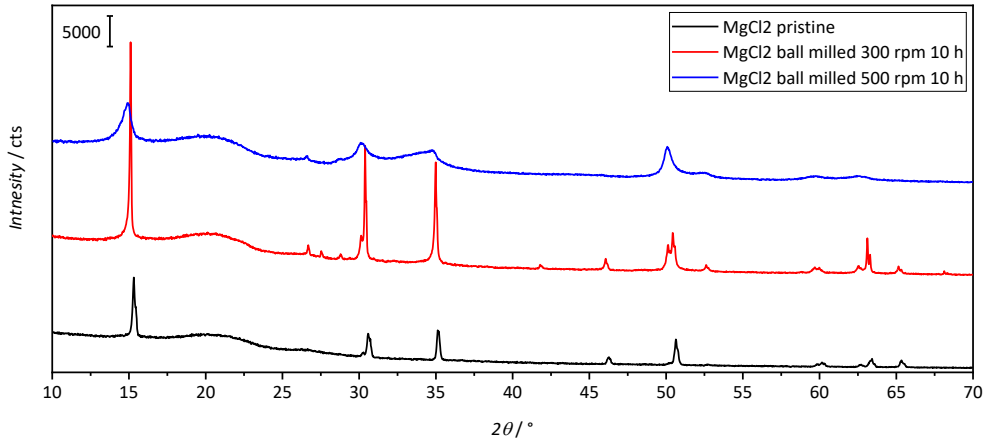

Figure 44 Comparison of XRD pattern from pristine crystallin $MgCl_2$ used as starting material, XRD pattern after first and second ball-milling.

7.2 Arrhenius plot for the repeated E_a measurements

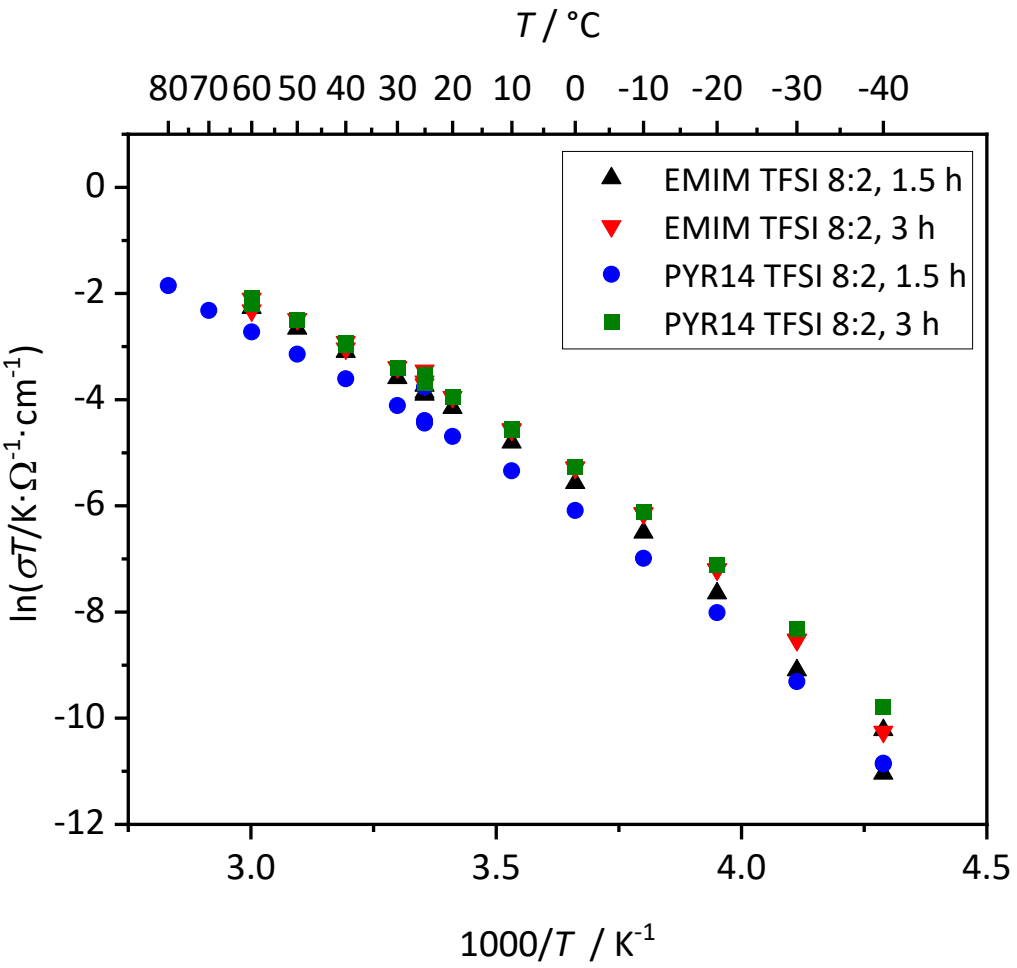

Figure 45 Arrhenius plots showing the temperature dependent conductivity of QSEs PYR14 and EMIM TFSI 8:2 for measurement with 1.5 h and 3 h equilibration time for each temperature.

Bibliographical index

[1]P. W. Gruber, P. A. Medina, G. A. Keoleian, S. E. Kesler, M. P. Everson, T. J. Wallington, *Journal of Industrial Ecology* **2011**, *15*, 760.

[2]G. R. Chapman, *Trans. Inst. Min. Metall., Sect. C* **2002**, *111*, 49.

[3]J. Muldoon, C. B. Bucur, T. Gregory, *Chem. Rev.* **2014**, *114*, 11683.

[4]H. Aono, E. Sugimoto: Y. Sadaoka, N. Imanak a, G. Adachi, *Solid State Ionics* **1991**, *47*, 257.

[5]H. W. Kim, P. Manikandan, Y. J. Lim, J. H. Kim, S. Nam, Y. Kim, *J. Mater. Chem. A* **2016**, *4*, 17025.

[6]A. Paolella, G. Bertoni, W. Zhu, D. Campanella, A. La Monaca, G. Girard, H. Demers, A. C. Gheorghe Nita, Z. Feng, A. Vijh et al., *J. Am. Chem. Soc.* **2022**, *144*, 3442.

[7]G. Pagot, K. Vezzù, S. G. Greenbaum, V. Di Noto, *J. Power Sources* **2021**, *493*, 229681.

[8]R. Davidson, A. Verma, D. Santos, F. Hao, C. Fincher, S. Xiang, J. van Buskirk, K. Xie, M. Pharr, P. P. Mukherjee et al., *ACS Energy Lett.* **2019**, *4*, 375.

[9]D. Aurbach, E. Zinigrad, Y. Cohen, H. Teller, *Solid State Ionics* **2002**, *148*, 405.

[10]A. J. Crowe, J. L. DiMeglio, K. K. Stringham, B. M. Bartlett, *J. Phys. Chem. C* **2017**, *121*, 20613.

[11]M. Matsui, *J. Power Sources* **2011**, *196*, 7048.

[12]Z. Lu, A. Schechter, M. Moshkovich, D. Aurbach, *J. Electroanal. Chem.* **1999**, *466*, 203.

[13]L. P. Lossius, F. Emmenegger, *Electrochim. Acta* **1996**, *41*, 445.

[14]O. Mizrahi, N. Amir, E. Pollak, O. Chusid, V. Marks, H. Gottlieb, L. Larush, E. Zinigrad, D. Aurbach, *J. Electrochem. Soc.* **2008**, *155*, A103.

[15]J. Luo, S. He, T. L. Liu, *ACS Energy Lett.* **2017**, *2*, 1197.

[16]O. Tutusaus, R. Mohtadi, T. S. Arthur, F. Mizuno, E. G. Nelson, Y. V. Sevryugina, *Angew. Chem.* **2015**, *127*, 8011.

[17]D. Aurbach, Z. Lu, A. Schechter, Y. Gofer, H. Gizbar, R. Turgeman, Y. Cohen, M. Moshkovich, E. Levi, *Nature* **2000**, *407*, 724.

[18]D. Aurbach, Y. Gofer, A. Schechter, O. Chusid, H. Gizbar, Y. Cohen, M. Moshkovich, R. Turgeman, *J. Power Sources* **2001**, *97-98*, 269.

[19]J. Genders, D. Pletcher, *e J. Electroanal. Chem. Interfacial Electrochem.* **1986**, *199*, 93.

[20]L. W. Gaddum, H. E. French, *J. Am. Chem. Soc.* **1927**, *49*, 1295.

[21]D. Aurbach, M. Moshkovich, A. Schechter, R. Turgeman, *Electrochem. Solid-State Lett.* **1999**, *3*, 31.

[22]C. Liebenow, *J. Appl. Electrochem.* **1997**, *27*, 221.

[23]T. Gregory, R. Hoffman, R. Winterton, *J. Electrochem. Soc.* **1990**, *137*, 775.

[24]A. Mayer, *J. Electrochem. Soc.* **1990**, *137*, 2806.

[25]D. Aurbach, G. S. Shivappa, E. Levi, A. Mitelman, O. Mizrahi, *Adv. Mater.* **2007**, *19*, 4260.

[26]J. L. Esbenshade, C. J. Barile, T. T. Fister, K. L. Bassett, P. Fenter, R. G. Nuzzo, A. A. Gewirth, *J. Phys. Chem. C* **2015**, *119*, 23366.

[27]J. Muldoon, C. B. Bucur, A. G. Oliver, J. Zajicek, G. D. Allred, W. C. Boggess, *Energy Environ. Sci.* **2013**, *6*, 482.

[28]R. Mohtadi, M. Matsui, T. S. Arthur, S.-J. Hwang, *Angew. Chem.* **2012**, *124*, 9918.

[29]Y.-S. Hu, *Nat. Energy* **2016**, *1*.

[30]J. Janek, W. G. Zeier, *Nat. Energy* **2016**, *1*.

[31]J. C. Bachman, S. Muy, A. Grimaud, H.-H. Chang, N. Pour, S. F. Lux, O. Paschos, F. Maglia, S. Lupart, P. Lamp et al., *Chem. Rev.* **2016**, *116*, 140.

[32]P. Stallworth, J. Fontanella, M. Wintersgill, C. D. Scheidler, J. J. Immel, S. Greenbaum, A. Gozdz, *J. Power Sources* **1999**, *81-82*, 739.

[33]N. Kamaya, K. Homma, Y. Yamakawa, M. Hirayama, R. Kanno, M. Yonemura, T. Kamiyama, Y. Kato, S. Hama, K. Kawamoto et al., *Nat. Mater.* **2011**, *10*, 682.

[34]Y. Seino, T. Ota, K. Takada, A. Hayashi, M. Tatsumisago, *Energy Environ. Sci.* **2014**, *7*, 627.

[35]M. Ue, *J. Electrochem. Soc.* **1994**, *141*, 3336.

[36]K. M. Diederichsen, E. J. McShane, B. D. McCloskey, *ACS Energy Lett.* **2017**, *2*, 2563.

[37]R. Murugan, V. Thangadurai, W. Weppner, *Angew. Chem. Int. Ed* **2007**, *46*, 7778.

[38]K. Kajihara, H. Nagano, T. Tsujita, H. Munakata, K. Kanamura, *J. Electrochem. Soc.* **2017**, *164*, A2183-A2185.

[39]P. G. Bruce, *Chemistry of Solid State Materials, 4*, Cambridge University Press, Cambridge, GBR, **2009**.

[40]N. K. Anuar, S. B. R. S. Adnan, M. H. Jaafar, N. S. Mohamed, *Ionics* **2016**, *22*, 1125.

[41]H. Aono, E. Sugimoto, Y. Sadaoka, N. Imanaka, G. Adachi, *J. Electrochem. Soc.* **1990**, *137*, 1023.

[42]D. McWhan, S. Allen., J. Remeika, P. Dernier, *Phys. Rev. Lett.*, *35*, 953.

[43]X. Sun, P. Bonnick, L. F. Nazar, *ACS Energy Lett.* **2016**, *1*, 297.

[44]H. D. Yoo, J. R. Jokisaari, Y.-S. Yu, B. J. Kwon, L. Hu, S. Kim, S.-D. Han, M. Lopez, S. H. Lapidus, G. M. Nolis et al., *ACS Energy Lett.* **2019**, *4*, 1528.

[45]S. Ikeda, M. Takahashi, J. Ishikawa, K. Ito, *Solid State Ionics* **1987**, *23*, 125-12.

[46]N. Imanaka, Y. Okazaki, G. Adachi, *J. Mater. Chem.* **2000**, *10*, 1431.

[47]N. Imanaka, Y. Okazaki, G. Adachi, *Ionics* **2001**, *7*, 440.

[48]J. Kawamura, K. Morota, N. Kuwata, Y. Nakamura, H. Maekawa, T. Hattori, N. Imanaka, Y. Okazaki, G. Adachi, *Solid State Commun.* **2001**, *120*, 295.

[49]S. Higashi, K. Miwa, M. Aoki, K. Takechi, *Chem. Commun. (Cambridge, U. K.)* **2014**, *50*, 1320.

[50]K. Kisu, S. Kim, M. Inukai, H. Oguchi, S. Takagi, S. Orimo, *ACS Appl. Energy Mater.* **2020**, *3*, 3174.

[51]A. Hayashi, S. Hama, H. Morimoto, M. Tatsumisago, T. Minami, *J. Am. Ceram. Soc.* **2001**, *84*, 477.

[52]F. Mizuno, A. Hayashi, K. Tadanaga, M. Tatsumisago, *Adv. Mater.* **2005**, *17*, 918.

[53]K. Minami, A. Hayashi, M. Tatsumisago, *J. Am. Ceram. Soc.* **2011**, *94*, 1779.

[54]A. Hayashi, K. Noi, A. Sakuda, M. Tatsumisago, *Nat. Commun.* **2012**, *3*, 856.

[55]T. Yamanaka, A. Hayashi, A. Yamauchi, M. Tatsumisago, *Solid State Ionics* **2014**, *262*, 601.

[56]P. Canepa, S.-H. Bo, G. Sai Gautam, B. Key, W. D. Richards, T. Shi, Y. Tian, Y. Wang, J. Li, G. Ceder, *Nat. Commun.* **2017**, *8*, 1759.

[57]L. Wang, Z. Zhao-Karger, F. Klein, J. Chable, T. Braun, A. R. Scher, C.-R. Wang, Y.-G. Guo, M. Fichtner, *ChemSusChem* **2019**, *12*, 2286.

[58]J. B. Goodenough, H. Y.-P. Hong, J. A. Kafalas, *Mater. Res. Bull.* **1976**, *11*, 203.

[59]H. Hong, *Mater. Res. Bull.* **1976**, *11*, 173.

[60]Z. Jian, Y.-S. Hu, X. Ji, W. Chen, *Adv. Mater.* **2017**, *29*.

[61]V. Pet'kov, V. Kurazhkovskaya, A. Orlova, M. Spiridonova, *Crystallogr. Rep.* **2002**, *47*, 802.

[62]V. I. Pet'kov, D. A. Lavrenov, M. V. Sukhanov, A. M. Koval'skii, E. Y. Borovikova, *Russ. J. Inorg. Chem.* **2019**, *64*, 1002.

[63]K. Nakano, Y. Noda, N. Tanibata, M. Nakayama, K. Kajihara, K. Kanamura, *RSC Adv.* **2019**, *9*, 12590.

[64]K. Nomura, S. Ikeda, K. Ito, H. Einaga, *J. Electroanal. Chem.* **1992**, *326*, 351.

[65]Z. A. Halim, S. Adnan, N. S. Mohamed, *Ceram. Int.* **2016**, *42*, 4452.

[66]M. Mustafa, M. Rani, S. Adnan, F. M. Salleh, N. S. Mohamed, *Ceram. Int.* **2020**, *46*, 28145.

[67]V. I. Pet'kov, A. S. Shipilov, E. Y. Borovikova, A. M. Kovalskii, I. A. Stenina, A. B. Yaroslavtsev, *Inorg. Mater.* **2018**, *54*, 1021.

[68]S. Barth, R. Olazcuaga, P. Gravereau, G. Le Flem, P. Hagenmuller, *Mater. Lett.* **1993**, *16*, 96.

[69]K. Makino, Y. Katayama, T. Miura, T. Kishi, *J. Power Sources* **2001**, *99*, 66.

[70]H. Takahashi, H. Takamura, *Mater. Trans.* **2012**, *53*, 932.

[71]E. R. Gobechiya, M. V. Sukhanov, V. I. Pet'kov, Y. K. Kabalov, *Crystallogr. Rep.* **2008**, *53*, 53.

[72]J. Hwang, K. Matsumoto, C.-Y. Chen, R. Hagiwara, *Energy Environ. Sci.* **2021**, *14*, 5834.

[73]W. Zhang, D. A. Weber, H. Weigand, T. Arlt, I. Manke, D. Schröder, R. Koerver, T. Leichtweiss, P. Hartmann, W. G. Zeier et al., *ACS Appl. Mater. Interfaces* **2017**, *9*, 17835.

[74]P. Thompson, D. Cox, J. Hastings, *J. Appl. Cryst.* **1987**, *20*, 79.

[75]L. W. Finger, *J. Appl. Cryst.* **1998**, *31*, 111.

[76]X. Qian, N. Gu, Z. Cheng, X. Yang, E. Wang, S. Dong, *J. Solid State Electrochem.* **2001**, *6*, 8.

[77]P. Hu, J. Ma, T. Wang, B. Qin, C. Zhang, C. Shang, J. Zhao, G. Cui, *Chem. Mater.* **2015**, *27*, 6668.

[78]S. Machill, T. Shodai, Y. Sakurai, J. Yamaki, *J. Solid State Electrochem.* **1999**, *3*, 97.

[79]J. Lee, Y.Xiao, Z. Liu, *Solid State Ionics* **2000**, *133*, 25.

[80]Y. Li, J. Li, *J. Phys. Chem. C* **2008**, *112*, 14216.

[81]O. Babushkina, *Z. Naturforsch.* **2008**, *63*, 66.

[82]M. Hesse, H. Meier, B. Zeeh, S. Bienz, L. Bigler, T. Fox, *Spektroskopische Methoden in der organischen Chemie*, Georg Thieme Verlag, Stuttgart, **2012**.

[83]G. Agarwal, J. D. Howard, V. Prabhakaran, G. E. Johnson, V. Murugesan, K. T. Mueller, L. A. Curtiss, R. S. Assary, *ACS Appl. Mater. Interfaces* **2021**, *13*, 38816.

[84]I. Shterenberg, M. Salama, H. D. Yoo, Y. Gofer, J.-B. Park, Y.-K. Sun, D. Aurbach, *J. Electrochem. Soc.* **2015**, *162*, A7118-A7128.

[85]G. Pagot, F. Bertasi, K. Vezzù, F. Sepehr, X. Luo, G. Nawn, E. Negro, S. J. Paddison, V. Di Noto, *Electrochim. Acta* **2017**, *246*, 914.

[86]T. Wada, A. Thakur, P. Chammingkwan, M. Terano, T. Taniike, A. Piovano, E. Groppo, *Catalysts* **2020**, *10*, 1089.